


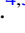


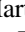
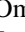


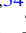
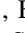
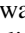




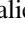
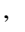

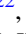

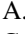

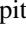

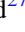

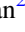
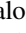

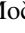

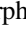
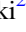
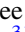
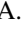



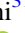


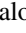


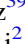



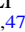

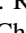
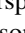





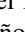


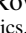



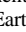
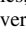
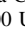






The TESS-Keck Survey. VIII. Confirmation of a Transiting Giant Planet on an Eccentric 261 Day Orbit with the Automated Planet Finder Telescope*

Paul A. Dalba^{1,2,52} , Stephen R. Kane² , Diana Dragomir³ , Steven Villanueva, Jr.^{4,53} , Karen A. Collins⁵ , Thomas Lee Jacobs^{6,54} , Daryll M. LaCourse^{7,54} , Robert Gagliano^{8,54} , Martti H. Kristiansen^{9,10} , Mark Omohundro^{11,54} , Hans M. Schwengeler^{12,54} , Ivan A. Terentev^{13,54} , Andrew Vanderburg⁴ , Benjamin Fulton¹⁴ , Howard Isaacson^{15,16} , Judah Van Zandt¹⁷ , Andrew W. Howard¹⁸ , Daniel P. Thorngren¹⁹ , Steve B. Howell²⁰ , Natalie M. Batalha¹ , Ashley Chontos^{21,55} , Ian J. M. Crossfield²² , Courtney D. Dressing¹⁵ , Daniel Huber²¹ , Erik A. Petigura¹⁷ , Paul Robertson²³ , Arpita Roy^{24,25} , Lauren M. Weiss²⁶ , Aida Behrard^{27,55} , Corey Beard²³ , Casey L. Brinkman²¹ , Steven Giacalone¹⁵ , Michelle L. Hill² , Jack Lubin²³ , Andrew W. Mayo^{15,28} , Teo Močnik²⁹ , Joseph M. Akana Murphy^{1,56} , Alex S. Polanski²² , Malena Rice^{30,55} , Lee J. Rosenthal¹⁸ , Ryan A. Rubenzahl^{18,55} , Nicholas Scarsdale¹ , Emma V. Turtelboom¹⁵ , Dakotah Tyler¹⁷ , Paul Benni^{31,54} , Pat Boyce³² , Thomas M. Esposito^{15,33} , E. Girardin^{34,54} , Didier Laloum^{35,54} , Pablo Lewin^{36,54} , Christopher R. Mann¹⁹ , Franck Marchis^{37,38} , Richard P. Schwarz³⁹ , Gregor Srdoc^{40,54} , Jana Steuer⁴¹ , Thirupathi Sivarani⁴² , Athira Unni⁴² , Nora L. Eisner⁴³ , Tara Fetherolf^{2,57} , Zhexing Li² , Xinyu Yao^{44,45} , Joshua Pepper⁴⁴ , George R. Ricker⁴ , Roland Vanderspek⁴ , David W. Latham⁵ , S. Seager^{4,46,47} , Joshua N. Winn⁴⁸ , Jon M. Jenkins²⁰ , Christopher J. Burke⁴ , Jason D. Eastman⁵ , Michael B. Lund⁴⁹ , David R. Rodriguez⁵⁰ , Pamela Rowden⁵¹ , Eric B. Ting²⁰ , and Jesus Noel Villaseñor⁴ 

¹ Department of Astronomy and Astrophysics, University of California, Santa Cruz, CA 95064, USA; pdalba@ucr.edu

² Department of Earth and Planetary Sciences, University of California Riverside, 900 University Avenue, Riverside, CA 92521, USA

³ Department of Physics & Astronomy, University of New Mexico, 1919 Lomas Boulevard NE, Albuquerque, NM 87131, USA

⁴ Department of Physics and Kavli Institute for Astrophysics and Space Research, Massachusetts Institute of Technology, Cambridge, MA 02139, USA

⁵ Center for Astrophysics | Harvard & Smithsonian, 60 Garden Street, Cambridge, MA 02138, USA

⁶ 12812 SE 69th Place, Bellevue, WA 98006, USA

⁷ 7507 52nd Place NE, Marysville, WA 98270, USA

⁸ Glendale, AZ 85308, USA

⁹ Brorfelde Observatory, Observator Gyldenkerne Vej 7, DK-4340 Tølløse, Denmark

¹⁰ DTU Space, National Space Institute, Technical University of Denmark, Elektrovej 327, DK-2800 Lyngby, Denmark

¹¹ Department of Physics, University of Oxford, Denys Wilkinson Building, Keble Road, Oxford OX1 3RH, UK

¹² Planet Hunter, Bottmingen, Switzerland

¹³ Planet Hunter, Petrozavodsk, Russia

¹⁴ NASA Exoplanet Science Institute/Caltech-IPAC, MC 314-6, 1200 East California Boulevard, Pasadena, CA 91125, USA

¹⁵ Department of Astronomy, University of California Berkeley, Berkeley, CA 94720, USA

¹⁶ Centre for Astrophysics, University of Southern Queensland, Toowoomba, QLD, Australia

¹⁷ Department of Physics & Astronomy, University of California Los Angeles, Los Angeles, CA 90095, USA

¹⁸ Department of Astronomy, California Institute of Technology, Pasadena, CA 91125, USA

¹⁹ Institute for Research on Exoplanets (iREx), Université de Montréal, Canada

²⁰ NASA Ames Research Center, Moffett Field, CA 94035, USA

²¹ Institute for Astronomy, University of Hawai'i, 2680 Woodlawn Drive, Honolulu, HI 96822, USA

²² Department of Physics & Astronomy, University of Kansas, 1082 Malott, 1251 Wescoe Hall Drive, Lawrence, KS 66045, USA

²³ Department of Physics & Astronomy, University of California Irvine, Irvine, CA 92697, USA

²⁴ Space Telescope Science Institute, 3700 San Martin Drive, Baltimore, MD 21218, USA

²⁵ Department of Physics and Astronomy, Johns Hopkins University, 3400 North Charles Street, Baltimore, MD 21218, USA

²⁶ Department of Physics, University of Notre Dame, Notre Dame, IN 46556, USA

²⁷ Division of Geological and Planetary Science, California Institute of Technology, Pasadena, CA 91125, USA

²⁸ Centre for Star & Planet Formation, Natural History Museum of Denmark & Niels Bohr Institute, University of Copenhagen, Øster Voldgade 5-7, DK-1350 Copenhagen K, Denmark

²⁹ Gemini Observatory/NSF's NOIRLab, 670 North A'ohoku Place, Hilo, HI 96720, USA

³⁰ Department of Astronomy, Yale University, New Haven, CT 06511, USA

³¹ Acton Sky Portal (Private Observatory), Acton, MA, USA

³² Boyce Research Initiatives and Education Foundation, 3540 Carleton Street, San Diego, CA 92106, USA

³³ SETI Institute, Carl Sagan Center, 189 Bernardo Avenue, Suite 200, Mountain View, CA 94043, USA

³⁴ Grand-Pra Private Observatory, 1984 Les Hauderes, Switzerland

³⁵ Observatoire Privé du Mont, 40280 Saint-Pierre-du-Mont, France

³⁶ The Maury Lewin Astronomical Observatory, Glendora, CA 91741, USA

³⁷ SETI Institute, Carl Sagan Center, 189 Bernardo Avenue, Mountain View, CA, USA

³⁸ Unistellar, 198 Alabama Street, San Francisco, CA 94110 USA

³⁹ Patashnick Voorheesville Observatory, Voorheesville, NY 12186, USA

⁴⁰ Kotizarovci Observatory, Sarsoni 90, 51216 Viskovo, Croatia

⁴¹ University Observatory Munich (USM), Scheinerstraße 1, D-81679 Munich, Germany

⁴² Indian Institute of Astrophysics, 2nd block Koramangala, Bangalore-34, India

⁴³ Department of Physics, University of Oxford, Keble Road, Oxford OX3 9UU, UK

⁴⁴ Department of Physics, Lehigh University, 16 Memorial Drive East, Bethlehem, PA 18015, USA

* Some of the data presented herein were obtained at the W. M. Keck Observatory, which is operated as a scientific partnership among the California Institute of Technology, the University of California, and the National Aeronautics and Space Administration. The Observatory was made possible by the generous financial support of the W. M. Keck Foundation.

⁴⁵ Shanghai Astronomical Observatory, Chinese Academy of Sciences, 80 Nandan Road, Shanghai 200030, People's Republic of China⁴⁶ Department of Earth, Atmospheric and Planetary Sciences, Massachusetts Institute of Technology, Cambridge, MA 02139, USA⁴⁷ Department of Aeronautics and Astronautics, MIT, 77 Massachusetts Avenue, Cambridge, MA 02139, USA⁴⁸ Department of Astrophysical Sciences, Princeton University, 4 Ivy Lane, Princeton, NJ 08544, USA⁴⁹ Caltech IPAC–NASA Exoplanet Science Institute, 1200 East California Avenue, Pasadena, CA 91125, USA⁵⁰ Space Telescope Science Institute, 3700 San Martin Drive, Baltimore, MD 21218, USA⁵¹ Royal Astronomical Society, Burlington House, Piccadilly, London W1J 0BQ, UK

Received 2021 September 24; revised 2021 November 19; accepted 2021 December 6; published 2022 January 13

Abstract

We report the discovery of TOI-2180 b, a $2.8 M_J$ giant planet orbiting a slightly evolved G5 host star. This planet transited only once in Cycle 2 of the primary Transiting Exoplanet Survey Satellite (TESS) mission. Citizen scientists identified the 24 hr single-transit event shortly after the data were released, allowing a Doppler monitoring campaign with the Automated Planet Finder telescope at Lick Observatory to begin promptly. The radial velocity observations refined the orbital period of TOI-2180 b to be 260.8 ± 0.6 days, revealed an orbital eccentricity of 0.368 ± 0.007 , and discovered long-term acceleration from a more distant massive companion. We conducted ground-based photometry from 14 sites spread around the globe in an attempt to detect another transit. Although we did not make a clear transit detection, the nondetections improved the precision of the orbital period. We predict that TESS will likely detect another transit of TOI-2180 b in Sector 48 of its extended mission. We use giant planet structure models to retrieve the bulk heavy-element content of TOI-2180 b. When considered alongside other giant planets with orbital periods over 100 days, we find tentative evidence that the correlation between planet mass and metal enrichment relative to stellar is dependent on orbital properties. Single-transit discoveries like TOI-2180 b highlight the exciting potential of the TESS mission to find planets with long orbital periods and low irradiation fluxes despite the selection biases associated with the transit method.

Unified Astronomy Thesaurus concepts: [Amateur astronomy \(35\)](#); [Extrasolar gaseous giant planets \(509\)](#); [Transit photometry \(1709\)](#); [Radial velocity \(1332\)](#); [Planetary interior \(1248\)](#)

Supporting material: machine-readable table

1. Introduction

Gas giant planets have been found to reside in many extrasolar planetary systems. The diversity in their sizes, masses, orbits, compositions, and formation pathways has been the subject of numerous studies. However, selection biases often cloud our understanding. For instance, the sensitivity of the transit method wanes for planets on orbits beyond a few tenths of an au owing to the inverse relation between transit probability and semimajor axis. Consequently, the vast majority of known exoplanets with $\gtrsim 1$ au orbits have been discovered via Doppler spectroscopy (e.g., Mayor et al. 2011; Fulton et al. 2021). Planet mass can be inferred from time series radial velocity (RV) observations but, without a transit, the planet radius and thereby bulk density remains unknown.

A critical component of the bulk composition for giant planets is the total mass of elements heavier than H and He (e.g., Guillot et al. 2006; Miller & Fortney 2011; Thorngren et al. 2016; Teske et al. 2019). This property is inferred using structural evolution models along with the measured planetary mass, radius, stellar age, and incident flux (e.g., Thorngren & Fortney 2019). Numerous theoretical planet formation studies have found that the correlation between the total mass of heavy elements in giant

planets—or, similarly, the metal enrichment relative to the host star—and planet mass is a useful tracer of planet formation processes (e.g., Mordasini et al. 2014; Hasegawa et al. 2018; Ginzburg & Chiang 2020; Shibata et al. 2020). Probing this giant planet mass–metallicity correlation along a third axis in orbital properties (i.e., period or separation) could prove informative. Yet previous efforts have simply not had a large enough sample size of giant planets on orbits wider than a few 0.1 au to conduct such an investigation (Miller & Fortney 2011; Thorngren et al. 2016).

Transit surveys such as the Kepler (Borucki et al. 2010; Thompson et al. 2018) and Transiting Exoplanet Survey Satellite (TESS; Ricker et al. 2015) missions occasionally detect giant planet candidates with orbital periods of 100–1000 days (e.g., Wang et al. 2015; Foreman-Mackey et al. 2016; Osborn et al. 2016; Uehara et al. 2016; Herman et al. 2019; Kawahara & Masuda 2019; Eisner et al. 2021). These candidates warrant close scrutiny, at least based on the $\sim 50\%$ false-positive rate for giant planets with similar orbits found for the Kepler mission (Santerne et al. 2014; Dalba et al. 2020a). Following vetting, long-term RV monitoring is often required to measure the planet mass, which then enables modeling of the bulk metallicity (e.g., Beichman et al. 2016; Dubber et al. 2019; Santerne et al. 2019; Dalba et al. 2021a, 2021b). TESS planets with orbital periods on the order of 100 days or more will typically be detected as single-transit events owing to the observational strategy of the TESS mission (e.g., LaCourse & Jacobs 2018; Villanueva et al. 2019; Díaz et al. 2020; Cooke et al. 2021). In this case, the RV monitoring is also necessary to determine the orbital period.

Here we describe the discovery and investigation of a 24 hr single-transit event observed for HD 238894, hereafter referred to as TOI-2180 b. The host star, TOI-2180 (TIC 298663873), is a bright ($V = 9.2$), slightly evolved G5 star. The confirmation of TOI-2180 b is notable relative to the current sample of TESS

⁵² NSF Astronomy and Astrophysics Postdoctoral Fellow.⁵³ Pappalardo Fellow.⁵⁴ Citizen Scientist.⁵⁵ NSF Graduate Research Fellow.⁵⁶ NSF Graduate Research Fellow, LSSTC Data Science Fellow.⁵⁷ UC Chancellor's Fellow.

exoplanets, including those identified as single transits, as it is the first to surpass an orbital period of 100 days.⁵⁸ In Section 2, we describe the TESS observations of TOI-2180, along with the follow-up photometric, imaging, and spectroscopic data sets. In Section 3, we discuss the consistency of the transit and RV data, which are then jointly modeled to determine the TOI-2180 system properties. We find that TOI-2180 b is a $2.7 M_J$ giant planet on a 261 day orbit with an orbital eccentricity of 0.368. In Section 4, we describe a global effort to detect an additional transit of TOI-2180 b from the ground. Although this effort failed to detect the transit, the nondetections provided a substantial improvement in precision on the orbital period. In Section 5, we determine the bulk heavy-element mass of TOI-2180 b. In Section 6, we use the long-term acceleration of TOI-2180 to place limits on the properties of a distant massive companion. In Section 7, we place TOI-2180 b in the context of other transiting giant planets and discuss the prospects for future characterization of the system. Lastly, in Section 8, we summarize our work.

2. Observations

2.1. TESS Photometry

TESS observed TOI-2180 (TIC 298663873) at a 2 minute (fast) cadence for the entirety of Cycle 2 of its primary mission (Sectors 14–26) and in Sectors 40 and 41 of its extended mission. The image data were processed by the Science Processing Operations Center at NASA Ames Research Center (Jenkins et al. 2016) to extract photometry from this target. A search for transiting planets failed to find a transit signature with two or more transits. Only a single transit event was observed in Sector 19 (2019 November 28 through 2019 December 22). This Sector 19 single transit was first identified by citizen scientists with the light-curve processing software `LcTools` (Schmitt et al. 2019), leading to early commencement of our RV follow-up campaign. In 2020 May, the Planet Hunters TESS collaboration (Eisner et al. 2020) announced this star as a community TESS object of interest (cTOI). In 2020 August, its disposition was elevated to TOI (Guerrero et al. 2021).

We downloaded the Sector 19 2 minute cadence light curve of TOI-2180 from the Mikulski Archive for Space Telescopes using the `lightkurve` package (Lightkurve Collaboration et al. 2018). We used the presearch data conditioning simple aperture photometry (PDCSAP) flux for which most of the high-frequency noise was removed (Smith et al. 2012; Stumpe et al. 2012, 2014). The PDCSAP light curve exhibited low-frequency noise features that we removed using a Savitzky–Golay filter after masking the clear transit event. The raw and flattened light curves, centered on the $\sim 0.5\%$ transit of TOI-2180 b, are shown in Figure 1.

Under the assumption of a circular central transit, Winn (2010, Equation (19)) showed how the transit duration (T) and stellar bulk density (ρ_*) can give an estimate of the orbital period (P) following

$$T \approx 13 \text{ hr} \left(\frac{P}{1 \text{ yr}} \right)^{1/3} \left(\frac{\rho_*}{\rho_\odot} \right)^{-1/3}, \quad (1)$$

⁵⁸ According to the list of confirmed TESS exoplanets in the NASA Exoplanet Archive (<https://exoplanetarchive.ipac.caltech.edu/index.html>) as of 2021 September 2.

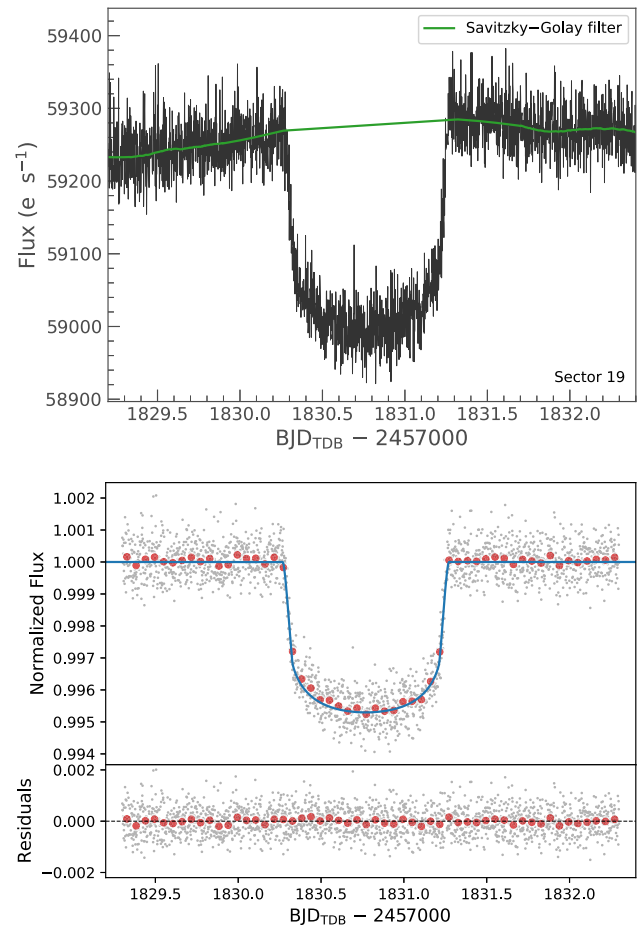


Figure 1. Single transit of TOI-2180 b observed by TESS with short cadence. Top: unflattened PDCSAP flux and the trend from the Savitzky–Golay filter. Bottom: flattened light curve. The red points are individual exposures (gray points) binned by a factor of 40. The blue line shows the best-fit transit model.

where P has units of years, and ρ_\odot is the solar bulk density. For $T = 24 \text{ hr}$ and $\rho_* = 0.335 \text{ g cm}^{-3}$ from the TESS Input Catalog (TIC; Stassun et al. 2019), Equation (1) gives $P \approx 547 \pm 111$ days assuming reasonable uncertainty in T and ρ_* . Combined with the nondetection of a matching transit event in the other Cycle 2 sectors, this possible orbital period suggested that TOI-2180 b was likely to be one of only a few long-period planets predicted to be detected by TESS through single-transit events (Villanueva et al. 2019).

2.2. Speckle Imaging

We acquired a high-resolution speckle image of TOI-2180 to search for nearby neighboring stars that might indicate the false-positive nature of the TESS single-transit event. We observed TOI-2180 on 2020 June 6 using the ‘Alopeke speckle instrument on the Gemini-North telescope⁵⁹ located on Maunakea in Hawai‘i. ‘Alopeke acquires an image of the star in a blue (562 nm) and a red (832 nm) band simultaneously. From these images, we derived contrast curves that show the limiting magnitude difference (Δm) in each band as a function of angular separation (Howell et al. 2011). As shown in Figure 2, we achieved an ~ 5 mag contrast at $0''.1$ and a

⁵⁹ <https://www.gemini.edu/instrumentation/alopeke-zorro>

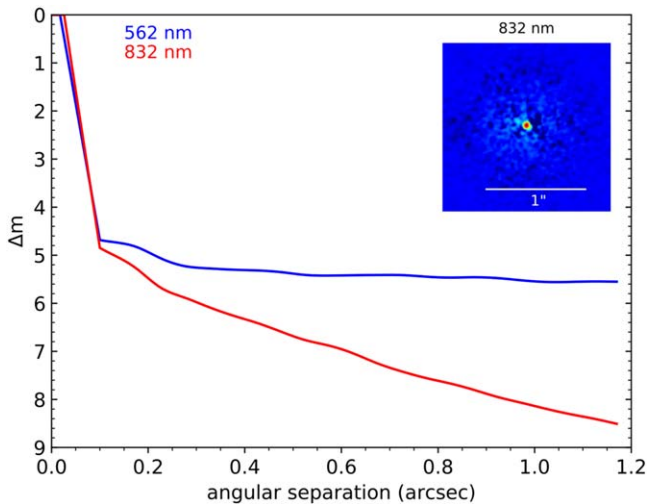


Figure 2. Limiting magnitudes (Δm) for the nondetection of a neighboring star based on the speckle imaging from ‘Alopeke. The inset shows the speckle image at 832 nm.

nondetection of sources with $\Delta m = 5\text{--}8.5$ within $1''/2$ of TOI-2180. Given the distance to TOI-2180 (116 pc; Table 2), a $0''/1$ projected separation corresponds to ~ 12 au. Although we cannot rule out a scenario whereby a luminous companion star was near conjunction with TOI-2180 at the time of our speckle observation, we assume in what follows that TOI-2180 is likely a single star. The speckle imaging nondetection suggests that any massive object in this system other than TOI-2180 b is likely to be a late M star or a substellar object.

The conclusion of TOI-2180 being a single star is further supported by the renormalized unit weight error (RUWE) as determined by Gaia Data Release (DR) 2 (Gaia Collaboration et al. 2018). The RUWE value for TOI-2180 is 1.01, which is typical of a single star (e.g., Belokurov et al. 2020).

2.3. Spectroscopy

Immediately following the discovery of the TESS single transit of TOI-2180, we began a Doppler monitoring campaign with the Automated Planet Finder (APF) telescope at Lick Observatory (Radovan et al. 2014; Vogt et al. 2014) as part of the TESS-Keck Survey (TKS). The TKS is a collaborative effort between the University of California, the California Institute of Technology, the University of Hawai‘i, and NASA aimed at providing multisite RV follow-up for many of the planetary systems discovered by TESS (e.g., Dai et al. 2020; Dalba et al. 2020b; Chontos et al. 2021; Lubin et al. 2021; Rubenzahl et al. 2021; Weiss et al. 2021). The APF uses the Levy Spectrograph, a high-resolution ($R \approx 114,000$) slit-fed optical echelle spectrometer (Radovan et al. 2010) that is ideal for bright ($V \leq 9$) stars such as TOI-2180 (Burt et al. 2015). The starlight passes through a heated iodine gas cell that allows for precise wavelength calibration and instrument profile tracking. The precise RV is inferred from each spectrum using a forward-modeling procedure (Butler et al. 1996; Fulton et al. 2015). Table 1 lists the RVs collected in our campaign.

In 2020 August, Lick Observatory and the APF shut down owing to nearby wildfires. To maintain our coverage of the emerging Keplerian RV signal, we temporarily conducted observations of TOI-2180 using the High Resolution Echelle Spectrometer (HIRES; Vogt et al. 1994) on the Keck I telescope at W. M. Keck Observatory. The reduction and

Table 1
RV Measurements of TOI-2180

BJD _{TDB}	RV (m s ⁻¹)	S_{HK}^a	Tel.
2,458,888.063868	-16.1 ± 3.9	0.1304 ± 0.0020	APF
2,458,894.911472	-29.1 ± 4.5	0.1476 ± 0.0020	APF
2,458,899.027868	-36.3 ± 3.8	0.1463 ± 0.0020	APF
2,458,906.015644	-43.6 ± 3.2	0.1093 ± 0.0020	APF
2,458,914.011097	-38.9 ± 3.3	0.1506 ± 0.0020	APF
2,458,954.765221	-59.0 ± 4.0	0.1468 ± 0.0020	APF
2,458,961.864505	-49.7 ± 4.3	0.1323 ± 0.0020	APF
2,458,964.879814	-53.3 ± 3.1	0.1298 ± 0.0020	APF
2,458,965.811833	-47.5 ± 4.2	0.1363 ± 0.0020	APF
2,458,966.879965	-65.9 ± 5.5	0.1204 ± 0.0020	APF

Note.

^a The S_{HK} values from APF and Keck data have different zero-points.

(This table is available in its entirety in machine-readable form.)

analysis procedure for Keck-HIRES spectra is broadly similar to that for data from the APF (e.g., Howard et al. 2010). The full version of Table 1 also contains the Keck-HIRES RVs of TOI-2180.

The time series RVs from both telescopes are shown in the top panel of Figure 3. Our 1.5 yr baseline captured two periods of a 261 day eccentric ($e \approx 0.4$) Keplerian signal, as well as a long-term acceleration. In Section 3, we will discuss the consistency of the RV data with the single transit from TESS and conduct a joint modeling of the system parameters.

Each RV measurement is accompanied by an estimate of stellar chromospheric activity approximated as the S_{HK} index (Isaacson & Fischer 2010). The indicators calculated for each instrument have different zero-points. The Pearson correlation coefficient between the S_{HK} indices and the RVs for APF and Keck are -0.10 (from 84 data points) and 0.68 (from 15 data points), respectively. Although the Keck data demonstrate a positive correlation significant to 3.3σ , the much larger APF data set shows no correlation ($<1\sigma$). Furthermore, we do not detect significant periodicity in the S_{HK} time series. Both of these findings suggest that the RV signals are not affected, or only minimally so, by stellar activity.

The extraction of the APF and Keck RVs relies on a high signal-to-noise ratio (S/N) template spectrum of TOI-2180 acquired with Keck-HIRES without the iodine cell (Butler et al. 1996). We also used this spectrum for a basic spectroscopic analysis of TOI-2180 with SpecMatch (Petigura 2015; Petigura et al. 2017). This analysis indicated that TOI-2180 has an effective temperature of $T_{\text{eff}} = 5739 \pm 100$ K, a surface gravity of $\log g = 4.00 \pm 0.10$, and a relative iron abundance (metallicity proxy) of $[\text{Fe}/\text{H}] = 0.25 \pm 0.06$ dex, consistent with a slightly evolved mid-G-type star. These values are in close agreement with those listed in the TIC (Stassun et al. 2019).

2.4. Ground-based Photometry

The single-transit detection for TOI-2180 by TESS and the subsequent RV follow-up effort allowed us to plan a ground-based photometry campaign with the goal of detecting another transit of TOI-2180 b. This campaign occurred in late August and early September of 2020, around the time of the first transit of TOI-2180 b since the one observed by TESS. We acquired 55 photometric data sets of TOI-2180 comprised of $\sim 20,000$ individual exposures spanning 11 days and 14 sites. Contributors

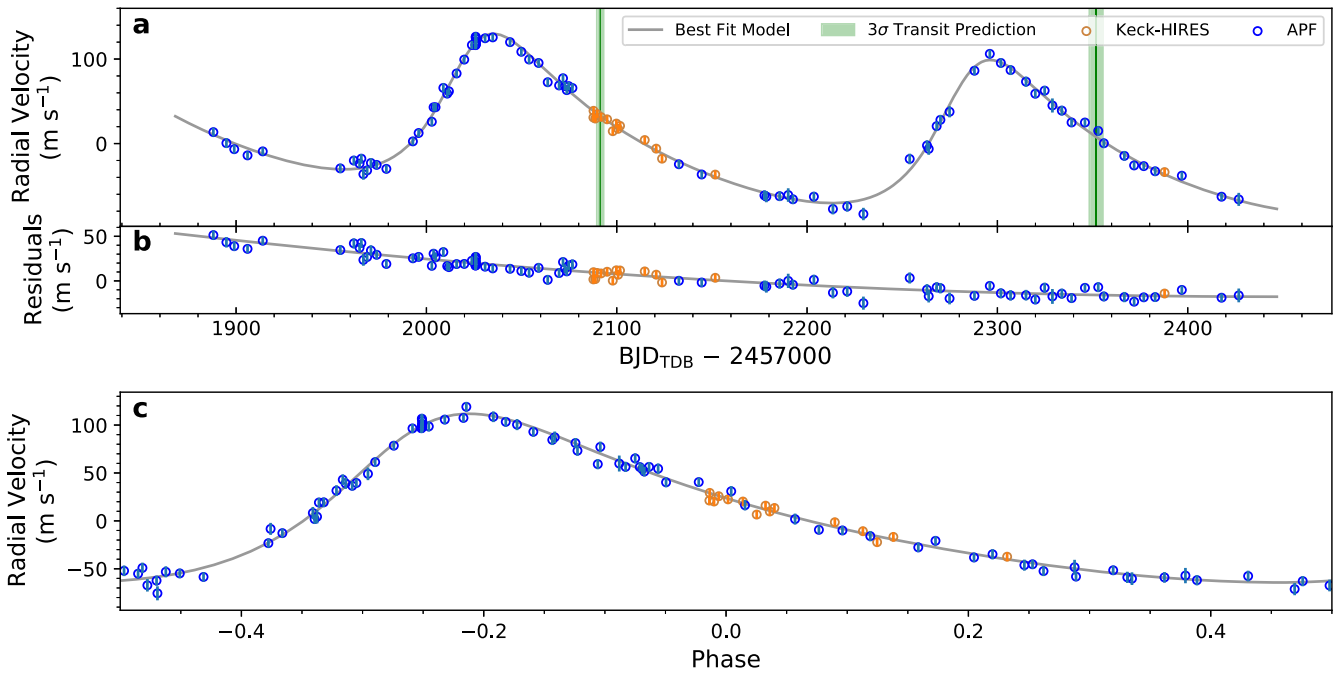


Figure 3. The RV measurements of TOI-2180. Panel (a): RV time series after subtraction of an offset velocity from each data set. Transit windows are shown in green. Panel (b): residuals between the RV time series and best-fit planet model not including acceleration terms. A quadratic trend is visible on top of the Keplerian signal from TOI-2180 b. Panel (c): phase-folded RVs after removal of the acceleration terms. A phase of zero corresponds to conjunction (transit).

to this campaign consisted of a mix of professional and amateur astronomers.

The quality of the ground-based telescope data sets varied widely. Some data achieved precision sufficient to rule out ingress or egress events for the relatively shallow (0.5%) transit of TOI-2180 b. Other data showed correlated noise or systematic errors several times this magnitude. We leave a detailed discussion of the individual observing sites for [Appendix](#). In Section 4, we will discuss our treatment of the ground-based data as a whole and our procedure for using it to refine the transit ephemeris of TOI-2180 b.

3. Modeling

3.1. Consistency between the Transit and the RV Data

A single-transit event only places a weak constraint on orbital period even under various simplifying assumptions (e.g., Yee & Gaudi 2008; Yao et al. 2021). We must therefore assess whether the same object caused the single transit and Doppler reflex motion of the host star.

In Section 2.1, we estimated that the duration of the single transit of TOI-2180 b and the stellar density listed in the TIC corresponded to a 547 day orbital period assuming a circular central transit. However, the RV measurements of TOI-2180 suggest a shorter period that has significant eccentricity. Depending on the argument of periastron (ω_*), orbital eccentricity can lead to shorter or longer transit duration compared to that from a circular orbit (e.g., Kane et al. 2012), which can bias the orbital period estimation from a single transit. Orbital eccentricity also increases the transit probability (Kane 2007), which is inherently low for objects with au-scale orbital distances.

We can account for eccentricity in our estimation of the orbital period to good approximation by including a factor of $\sqrt{1 - e^2}/(1 + e \sin \omega_*)$ on Equation (1) (Winn 2010). We

determined e and ω_* by conducting a Keplerian model fit to the APF and Keck RVs using the `RadVel` modeling tool kit⁶⁰ (Fulton et al. 2018). In this fit, we applied a normal prior on the time of conjunction ($\text{BJD}_{\text{TDB}} = 2,458,830.79 \pm 0.05$) using the transit timing from the Planet Hunters TESS characterization of the single transit (Eisner et al. 2021). The fit converged quickly, and we found that $e = 0.367 \pm 0.0074$, $\omega_* = -0.76 \pm 0.023$ rad, and $P = 260.68 \pm 0.54$ days. This argument of periastron corresponds to a time of periastron that is 70.0 ± 1.2 days prior to transit. Therefore, at the time of transit, the orbital velocity of TOI-2180 b is decreasing.

Reevaluating Equation (1) with the factor to account for an eccentric orbit gives 283 ± 59 days, which is consistent with the period of the Keplerian signal in the RVs. Considering the uncertainty introduced by the transit impact parameter could further explain the difference between this orbital period estimate and the observed 261 day period. This result demonstrates self-consistency with our assumption of a T_0 value in the `RadVel` fit. Therefore, we continue our analysis with the implicit assumption that the single transit in the photometry and the Keplerian signal in the RVs can be ascribed to the same planet: TOI-2180 b.

3.2. Comprehensive System Modeling

We modeled the stellar and planetary parameters for the TOI-2180 system using the `EXOFASTv2` modeling suite (Eastman et al. 2013, 2019). We include the TESS single-transit photometry, all of the RVs from Keck-HIRES and APF-Levy, and archival broadband photometry of TOI-2180 from Gaia DR2 (Gaia Collaboration et al. 2018), the Two Micron All Sky Survey (Cutri et al. 2003), and the Wide-field Infrared Survey Explorer (Cutri et al. 2014). `EXOFASTv2` computes spectral energy distributions (SEDs) from MIST models and

⁶⁰ <https://radvel.readthedocs.io/>

Table 2

Median Values and 68% Confidence Intervals for the Stellar Parameters for TOI-2180

Parameter	Units	Values
Informative Priors		
T_{eff}	Effective temperature (K)	$\mathcal{N}(5739, 115)$
[Fe/H]	Metallicity (dex)	$\mathcal{N}(0.25, 0.06)$
ϖ	Parallax (mas)	$\mathcal{N}(8.597, 0.017)$
A_V	V-band extinction (mag)	$\mathcal{U}(0, 0.1376)$
Stellar Parameters		
M_*	Mass (M_\odot)	$1.111^{+0.047}_{-0.046}$
R_*	Radius (R_\odot)	$1.636^{+0.033}_{-0.029}$
L_*	Luminosity (L_\odot)	$2.544^{+0.091}_{-0.093}$
F_{bol}	Bolometric flux (cgs)	$6.01 \times 10^{-9} \text{ }^{+2.1 \times 10^{-10}}_{-2.2 \times 10^{-10}}$
ρ_*	Density (g cm^{-3})	$0.359^{+0.015}_{-0.016}$
$\log g$	Surface gravity (cgs)	$4.057^{+0.015}_{-0.016}$
T_{eff}	Effective temperature (K)	5695^{+58}_{-60}
[Fe/H]	Metallicity (dex)	0.253 ± 0.057
[Fe/H] ₀	Initial metallicity ^a (dex)	$0.269^{+0.055}_{-0.054}$
Age	Age (Gyr)	$8.1^{+1.5}_{-1.3}$
EEP	Equal evolutionary phase ^b	$452.1^{+3.9}_{-5.0}$
A_V	V-band extinction (mag)	$0.077^{+0.041}_{-0.048}$
σ_{SED}	SED photometry error scaling	$0.69^{+0.24}_{-0.16}$
ϖ	Parallax (mas)	8.597 ± 0.017
d	Distance (pc)	116.32 ± 0.23

Notes. See Table 3 in Eastman et al. (2019) for a detailed description of all parameters and default (noninformative) priors beyond those specified here. The $\mathcal{N}(a, b)$ denotes a normal distribution with mean a and variance b^2 , and $\mathcal{U}(a, b)$ denotes a uniform distribution over the interval $[a, b]$.

^a Initial metallicity is that of the star when it formed.

^b Corresponds to static points in a star's evolutionary history. See Section 2 of Dotter (2016).

the Gaia parallax measurements and fits them to the archival photometry to infer the properties of the host star. We placed normal priors on T_{eff} and [Fe/H] based on the SpecMatch analysis of the high-S/N template spectrum of TOI-2180 (Section 2.3). The width of the T_{eff} prior was inflated to 115 K (2%), and a noise floor of 2% was applied to the bolometric flux used in the SED determination to account for systematic uncertainties inherent in the MIST models (Tayar et al. 2020). We also placed a uniform prior on extinction ($A_V \leq 0.1376$) using the galactic dust maps of Schlafly & Finkbeiner (2011) and a normal prior on parallax ($\varpi = 8.597 \pm 0.017$ mas) using the Gaia DR3 measurement corrected for the zero-point offset (Gaia Collaboration et al. 2021; Lindegren et al. 2021). These priors are summarized at the top of Table 2.

We gauged convergence of the EXOFASTv2 fit by the number of independent draws (Ford 2006), which exceeded 1000, and the Gelman–Rubin statistic (Gelman & Rubin 1992), which was smaller than 1.01, for every fitted parameter. From the fit parameters, numerous properties of TOI-2180 b were derived. Table 3 lists all relevant planetary parameters for TOI-2180 b. The derived planetary radius and transit depth assume no oblateness (e.g., Seager & Hui 2002) and no system of rings (e.g., Barnes & Fortney 2004; Akınsanmi et al. 2018), although TOI-2180 b could plausibly have both.

The TESS data and the best-fit transit model are shown in Figure 1. All RV data and the best-fit RV model are shown in Figure 3. We included a quadratic function of time in the fit to account for the force from an additional planet or star on TOI-2180. Both coefficients in the quadratic function are greater

Table 3

Median Values and 68% Confidence Interval of the Planet Parameters for TOI-2180 b

Parameter	Units	Values
Planetary Parameters		
P	Period ^a (days)	$260.79^{+0.59}_{-0.58}$
R_P	Radius (R_J)	$1.010^{+0.022}_{-0.019}$
M_P	Mass (M_J)	$2.755^{+0.087}_{-0.081}$
T_C	Time of conjunction (BJD _{TDB})	$2,458,830.7652 \pm 0.0010$
a	Semimajor axis (au)	0.828 ± 0.012
i	Inclination (deg)	$89.955^{+0.032}_{-0.044}$
e	Eccentricity	0.3683 ± 0.0073
ω_*	Argument of periastron (deg)	-43.8 ± 1.3
T_{eq}	Equilibrium temperature ^b (K)	$348.0^{+3.3}_{-3.6}$
τ_{circ}	Tidal circularization time-scale (Gyr)	$54,600,000^{+3,800,000}_{-4,500,000}$
K	RV semiamplitude (m s^{-1})	$87.75^{+0.98}_{-0.99}$
$\dot{\gamma}$	RV slope ^c ($\text{m s}^{-1} \text{ day}^{-1}$)	-0.1205 ± 0.0043
$\ddot{\gamma}$	RV quadratic term ^c ($\text{m s}^{-1} \text{ day}^{-2}$)	$0.000214^{+0.000039}_{-0.000038}$
δ_{TESS}	Transit depth in TESS band	$0.004766^{+0.000078}_{-0.000076}$
τ	Ingress/egress transit duration (days)	$0.06044^{+0.0019}_{-0.00063}$
T_{14}	Total transit duration (days)	$1.0040^{+0.0032}_{-0.0031}$
b	Transit impact parameter	$0.100^{+0.095}_{-0.070}$
ρ_P	Density (g cm^{-3})	$3.32^{+0.14}_{-0.16}$
$\log g_P$	Surface gravity (cgs)	$3.827^{+0.012}_{-0.015}$
$\langle F \rangle$	Incident flux ($10^9 \text{ erg s}^{-1} \text{ cm}^{-2}$)	0.00442 ± 0.00018
T_P	Time of periastron (BJD _{TDB})	$2,458,760.7 \pm 1.3$
T_S	Time of eclipse (BJD _{TDB})	$2,458,745.41^{+1.00}_{-1.0}$
b_S	Eclipse impact parameter	$0.060^{+0.056}_{-0.042}$
τ_S	Ingress/egress eclipse duration (days)	$0.03593^{+0.00098}_{-0.00088}$
$T_{S,14}$	Total eclipse duration (days)	0.599 ± 0.013
$\delta_{S,2.5\mu\text{m}}$	Blackbody eclipse depth at 2.5 μm (ppm)	$0.00237^{+0.00034}_{-0.00032}$
$\delta_{S,5.0\mu\text{m}}$	Blackbody eclipse depth at 5.0 μm (ppm)	1.54 ± 0.10
$\delta_{S,7.5\mu\text{m}}$	Blackbody eclipse depth at 7.5 μm (ppm)	$11.29^{+0.49}_{-0.50}$
TESS Parameters		
u_1	Linear limb-darkening coefficient	0.316 ± 0.029
u_2	Quadratic limb-darkening coefficient	0.248 ± 0.044
APF-Levy Parameters		
γ_{rel}	Relative RV offset ^c (m s^{-1})	$-30.0^{+1.2}_{-1.3}$
σ_J	RV jitter (m s^{-1})	$4.16^{+0.67}_{-0.62}$
Keck-HIRES Parameters		
γ_{rel}	Relative RV offset ^c (m s^{-1})	$-12.7^{+1.4}_{-1.5}$
σ_J	RV jitter (m s^{-1})	$4.86^{+1.3}_{-0.93}$

Notes. See Table 3 in Eastman et al. (2019) for a detailed description of all parameters and default (noninformative) priors.

^a This orbital period is derived from the full posterior from the EXOFASTv2 fit. See Section 4 for a description of the likely orbital period values ($260.18^{+0.19}_{-0.30}$ or $261.76^{+0.29}_{-0.16}$ days) after the ground-based photometric transit recovery campaign for TOI-2180.

^b Assumes a Jupiter-like Bond albedo (0.34) and perfect heat redistribution.

^c Reference epoch = 2,459,157.439110.

than 5σ discrepant from zero, suggesting that there is indeed a long-term variation in the RVs. Even with more than a 500 day baseline of observations, we do not sample enough of the long-

term signal to determine its cause. The lack of correlation between the RVs and the S_{HK} activity indicators disfavors stellar activity as the true explanation (Section 2.3). Instead, we suggest that another massive object is orbiting TOI-2180 (Section 6).

Owing to the well-sampled time series of precise RVs, the posterior for the orbital period for the single transit TOI-2180 b has a standard deviation below 1 day (0.23%) that is well characterized by a normal distribution. In the following section, we will further constrain the orbital period of TOI-2180 b based on ground-based photometry acquired near the timing of an additional transit.

4. Ephemeris Refinement from Ground-based Observations

With each new RV we acquired of TOI-2180, we calculated the timing of the next transit of TOI-2180 b. The second transit (i.e., the first transit to occur since the TESS single transit) occurred at some point in late August or early September of 2020. At that time, the 2σ transit window—which was almost entirely determined by the uncertainty on orbital period—was approximately 10 days wide.⁶¹

We attempted the formidable task of observing this 24 hr long, relatively shallow (0.5%) transit by planning a global ground-based photometry campaign. In total, 15 telescopes acquired 55 data sets containing over 20,000 individual exposures of TOI-2180 spanning 11 days. These included professional observatories, amateur observatories, and two portable digital eVscope telescopes. Each data set was processed with standard differential aperture photometry using background stars as references. Basic information about each telescope is provided in Appendix, a summary of each observation is listed in Table 4, and all data are plotted in Figure 9.

None of the observations provided a conclusive detection of a TOI-2180 b transit. As has been the case for other attempts to detect transits of long-period planets (e.g., Winn et al. 2009; Dalba & Muirhead 2016; Dalba & Tamburo 2019), any single observation could only observe out-of-transit baseline and ingress or egress at best. This photometric signature can be easily mimicked by flux variations between the target and reference stars as the airmass changed. On the other hand, owing to the duration of the transit and the difficulty of absolute flux calibration at the precision of the transit depth, distinguishing a fully in-transit observation from a fully out-of-transit one is challenging. Also, the $\sim 0.5\%$ transit depth was on the order of the noise floor for many of the sites. All of these factors contributed to the nondetection.

However, despite the lack of an obvious transit detection, we developed a straightforward method to refine the orbital period of TOI-2180 b by simultaneously searching all data sets for times where ingress or egress did not occur to high statistical significance. Ruling out these times rules out chunks of the orbital period posterior. Conversely, at times when we cannot determine if ingress or egress occurred—or if ingress or egress even appears to be favored by the data—we do not rule out those portions of the posterior.

We began with the relative light curves for each data set, which were the aperture flux values of TOI-2180 divided by the

aperture flux of one or more reference stars. We sigma-clipped the relative light curves for 4σ outliers and normalized each to its median. So far, we had not attempted to remove flux variations due to airmass. Our first task was to remove data sets with high scatter to avoid introducing spurious results in the ephemeris refinement. Although even imprecise data contain useful information, we found that many of the high-scatter data sets contained time-correlated noise or systematic noise features. Instead of attempting to correct for these noise properties, we chose to exclude the data set entirely. For the purpose of this procedure, we fit and subtracted an airmass model,

$$F'(t) = c_1 e^{-c_2 X(t)}, \quad (2)$$

where F' is the flux variation owing to a varying airmass X , both of which are functions of time t . The model had two fitted coefficients, c_1 and c_2 , which can have any finite value. After this airmass correction, data sets for which the standard deviation exceeded the transit depth (0.5%) were removed (gray points in Figure 9). We list this standard deviation for each data set in Table 4.

Next, we established a fine linear grid of mid-transit (T_0) times that spanned fourth contact at the time of the very first flux measurement ($\text{BJD}_{\text{TDB}} = 2,459,085.674949$) to first contact at the time of our very last flux measurement ($\text{BJD}_{\text{TDB}} = 2,459,096.875975$). These T_0 values were used to generate transit models that were compared with the data. Each value of T_0 maps to a unique value of the orbital period.

Then, we iterated over each T_0 value and data set conducting the following procedure. A transit model was generated at that T_0 using the `batman` package (Kreidberg 2015). All other transit parameters were fixed at the values derived from the EXOFASTv2 model (Table 3), except for the quadratic limb-darkening coefficients, which were drawn from the lookup tables of Claret & Bloemen (2011) according to filter. We subtracted this transit model from the relative light curve that was sigma-clipped and normalized to its median. Note that the light curve in this case had not been corrected for airmass variations, which were therefore still present after the subtraction. The model-subtracted light curve was then fit to Equation (2) with a basic least-squares algorithm that minimized the χ^2 statistic.

Consider the logic behind this procedure. If the airmass model is a good fit to the light curve after the transit model is subtracted (i.e., low χ^2 value), then we failed to rule out the transit at that time. We also cannot confidently claim that we have detected the transit, since the good fit to the airmass model could be coincidental. In this case, the probability of this transit time is still described by the posterior from the RV and transit joint fit. Conversely, if the airmass model is a poor fit to the light curve after the transit model is subtracted (i.e., high χ^2 value), then we can be confident that the transit did not occur at that time.

Each T_0 for each data set yielded its own minimum χ^2 value from which we calculated the corresponding log likelihood value (i.e., the maximum of the likelihood function) and Bayesian information criterion (BIC; Schwarz 1978). We then summed the BIC values across data sets to produce a total BIC as a function of T_0 and hence orbital period.

We also repeated our entire procedure and calculated the same metrics assuming that none of the observations sampled the transit. In this “no-transit” scenario, the transit occurred

⁶¹ Note that the uncertainty for orbital period reported in Table 3 is informed by the full RV data set and is therefore much smaller than the corresponding estimate in 2020 August.

Table 4
Summary of Ground-based Photometry of TOI-2180

Tel. ID	UTC Date	Start Time ^a	Stop Time ^a	Filter	Exp. Time (s)	σ (ppt) ^b	N_{obs} ^c	Observer/Contact	Figure 9 ^d
MLO	2020 Aug 24	0.674949	0.910757	<i>B</i>	15	7.9	967	Lewin	...
SCT	2020 Aug 24	1.334491	1.439421	TESS	20	4.5	255	Srdoc	a-Orange
RCO	2020 Aug 24	1.357160	1.569239	<i>zs</i>	15	4.7	548	Girardin	a-Blue
BARO	2020 Aug 25	1.669737	1.907806	<i>i'</i>	3	16.7	373	Boyce	...
LCOGT-HAL	2020 Aug 25	1.735700	1.961921	<i>zs</i>	60	7.4	241	Collins	...
SCT	2020 Aug 25	2.316263	2.554778	TESS	20	4.0	624	Srdoc	b-Green
MLO	2020 Aug 26	2.652399	2.976117	<i>I</i>	24	5.0	811	Lewin	b-Orange
BARO	2020 Aug 26	2.715152	2.899239	<i>i'</i>	3	12.2	289	Boyce	...
LCOGT-HAL	2020 Aug 26	2.734919	2.896656	<i>B</i>	30	14.3	281	Collins	...
RCO	2020 Aug 26	3.342047	3.593955	<i>zs</i>	15	5.7	695	Girardin	...
LCOGT-McD	2020 Aug 27	3.599088	3.819390	<i>zs</i>	20	1.5	325	Collins	b-Blue
MLO	2020 Aug 27	3.641554	3.918703	<i>I</i>	24	5.2	731	Lewin	...
W43	2020 Aug 27	4.305405	4.619606	<i>r'</i>	5	7.6	550	Steuer	...
SCT	2020 Aug 27	4.326957	4.554686	TESS	20	4.0	535	Srdoc	c-Brown
OPM	2020 Aug 27	4.354370	4.557354	<i>I</i>	25	8.9	133	Laloum	...
RCO	2020 Aug 27	4.383018	4.503405	<i>zs</i>	15	3.6	364	Girardin	c-Purple
LCOGT-TFN	2020 Aug 27	4.397824	4.568805	<i>i'</i>	30	5.6	281	Schwarz, Dragomir	...
DRA	2020 Aug 28	4.626313	4.917531	<i>r'</i>	15	3.3	318	Mann	c-Orange
DRA	2020 Aug 28	4.626314	4.917550	<i>g'</i>	15	3.6	427	Mann	c-Blue
BARO	2020 Aug 28	4.661461	4.894461	<i>i'</i>	3	11.5	356	Boyce	...
MLO	2020 Aug 28	4.713041	4.964718	<i>I</i>	25	6.4	604	Lewin	...
eV-A	2020 Aug 28	4.716616	4.878179	Clear	3.97	5.7	121	Dalba	...
eV-B	2020 Aug 28	4.717048	4.876957	Clear	3.97	5.0	101	Dalba	...
HCT	2020 Aug 28	5.137385	5.328852	<i>R</i>	15	5.4	359	Unni, Thirupathi	...
JCB	2020 Aug 28	5.203377	5.283490	<i>R</i>	30	3.0	63	Unni, Thirupathi	c-Green
LCOGT-TFN	2020 Aug 28	5.399757	5.566928	<i>i'</i>	30	6.6	279	Schwarz, Dragomir	...
MLO	2020 Aug 29	5.638188	5.898637	<i>I</i>	25	4.5	659	Lewin	c-Red
eV-B	2020 Aug 29	5.648009	5.876296	Clear	3.97	8.4	119	Dalba	...
BARO	2020 Aug 29	5.656000	5.892000	<i>i'</i>	3	12.9	367	Boyce	...
eV-A	2020 Aug 29	5.662142	5.876826	Clear	3.97	7.3	112	Dalba	...
JCB	2020 Aug 29	6.167566	6.270573	<i>R</i>	50	4.4	83	Unni, Thirupathi	d-Orange
eV-B	2020 Aug 30	6.635574	6.872570	Clear	3.97	6.0	159	Dalba	...
MLO	2020 Aug 30	6.638204	6.910475	<i>I</i>	25	4.9	691	Lewin	d-Green
eV-A	2020 Aug 30	6.720113	6.872948	Clear	3.97	6.1	101	Dalba	...
BARO	2020 Aug 30	6.779452	6.888816	<i>i'</i>	3	14.1	172	Boyce	...
ASP	2020 Aug 31	7.544901	7.766374	<i>r'</i>	10	4.2	1174	Benni	d-Blue
eV-B	2020 Aug 31	7.629679	7.863857	Clear	3.97	5.4	148	Dalba	...
eV-A	2020 Aug 31	7.630012	7.845392	Clear	3.97	4.3	118	Dalba	d-Red
MLO	2020 Aug 31	7.679966	7.917370	<i>I</i>	25	5.1	597	Lewin	...
BARO	2020 Aug 31	7.692682	7.885739	<i>i'</i>	3	12.8	299	Boyce	...
eV-B	2020 Sep 01	8.626611	8.871359	Clear	3.97	6.6	149	Dalba	...
MLO	2020 Sep 01	8.637218	8.636640	<i>I</i>	40	3.8	422	Lewin	e-Orange
eV-A	2020 Sep 01	8.638064	8.871871	Clear	3.97	5.3	151	Dalba	...
BARO	2020 Sep 01	8.698078	8.883357	<i>i'</i>	3	15.2	293	Boyce	...
SCT	2020 Sep 01	9.304464	9.545086	TESS	20	5.0	649	Srdoc	...
OPM	2020 Sep 01	9.352277	9.569774	<i>I</i>	40	5.5	297	Laloum	...
LCOGT-McD	2020 Sep 02	9.594154	9.681363	<i>zs</i>	20	2.1	123	Collins	e-Blue
MLO	2020 Sep 02	9.630824	9.925402	<i>I</i>	40	4.1	519	Lewin	e-Green
DRA	2020 Sep 02	9.631545	9.887763	<i>r'</i>	15	6.0	504	Mann	...
DRA	2020 Sep 02	9.631549	9.904950	<i>g'</i>	15	5.9	595	Mann	...
LCOGT-HAL	2020 Sep 02	9.730071	9.900129	<i>i'</i>	30	7.3	276	Schwarz	...
BARO	2020 Sep 02	9.752900	9.880042	<i>i'</i>	3	20.7	200	Boyce	...
MLO	2020 Sep 04	10.695742	10.907067	<i>I</i>	50	3.0	307	Lewin	f-Orange
LCOGT-HAL	2020 Sep 03	10.729537	10.938998	<i>i'</i>	30	4.6	355	Schwarz, Dragomir	f-Blue
BARO	2020 Sep 04	11.769168	11.875975	<i>i'</i>	3	12.9	170	Boyce	...

Notes.^a Start and stop times are listed with respect to 2,459,085 BJD_{TDB}.^b The σ value is the standard deviation of the flux in parts per thousand (ppt) after the airmass correction.^c The number of observations in each data set (N_{obs}) is calculated after sigma clipping.^d A combination of a letter and a color indicates that this data set was used in the ephemeris refinement of TOI-2180 b (Section 4) and is shown in that particular color and panel of Figure 9. A value of “...” indicates that this data set was not used in the analysis.

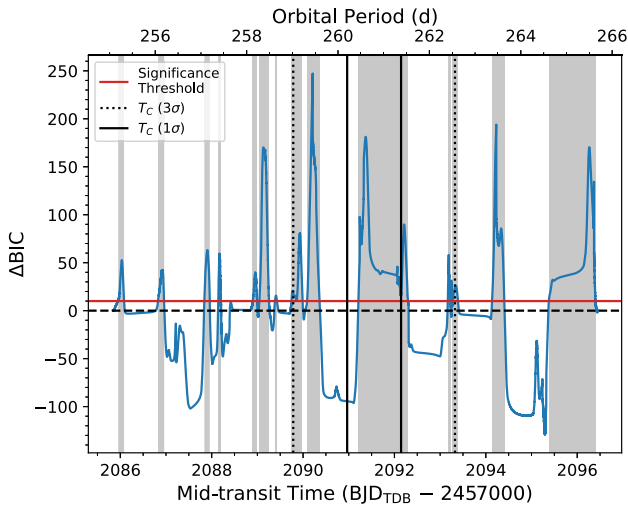


Figure 4. Summary of the transit ephemeris refinement analysis. Positive values of ΔBIC indicate mid-transit times that are disfavored relative to a nondetection. We consider mid-transit times with $\Delta\text{BIC} \geq 10$ (gray regions) to be ruled out by the ground-based photometry. Negative values of ΔBIC indicate times where the transit model provided a good fit. However, this could be coincidental, and we do not interpret a large negative ΔBIC as evidence of the transit. The 1σ and 3σ ranges for mid-transit time (T_C) from the final ephemeris (Table 3) are shown as vertical lines. Each mid-transit time corresponds to a specific orbital period of TOI-2180 b, as indicated at the top of the figure.

either before or after the observations or fell entirely within a data gap.

In Figure 4, we show the difference in BIC values (ΔBIC) between the transit and no-transit scenarios as a function of mid-transit time. The earliest and latest values of ΔBIC approach zero, as expected. Values of T_0 with substantially negative ΔBIC primarily correspond to times when ingress and/or egress occurred during data gaps, and the relatively flat ground-based photometry mimics the basin of a transit. On the other hand, values of T_0 with substantially positive ΔBIC correspond to ingress and/or egress lining up with ground-based photometry that clearly does not contain such features. We adopted a ΔBIC threshold of 10—corresponding to “very strong” evidence against the transit model (Kass & Raftery 1995)—to determine which values of T_0 we could rule out (Figure 4, gray regions) and mapped this refinement back to the orbital period. The resulting trimmed posterior for the orbital period is shown in Figure 5.

The ground-based transit detection campaign served to broadly divide the normal posterior for the orbital period into two smaller, non-Gaussian groups while ruling out the median and most likely values of the original distribution. Described by their median and 68% credible intervals, the two possible orbital periods are $260.18^{+0.19}_{-0.30}$ and $261.76^{+0.29}_{-0.16}$ days.

To assess the efficiency of the ground-based photometry campaign, we consider the duty cycle between exposure time and orbital period posterior time to be ruled out. Multiplying the number of exposures by their respective exposure times (Table 4) for all observations (regardless of whether they were excluded from this analysis) yields 4.4 days. The aforementioned ΔBIC threshold of 10 rules out 3.8 days worth of orbital period posterior space. Therefore, the duty cycle of the campaign was 86% (i.e., for every 1 hr of exposure time, we ruled out 52 minutes of orbital period). Ideally, a campaign like this would detect the transit, and the duty cycle would be less

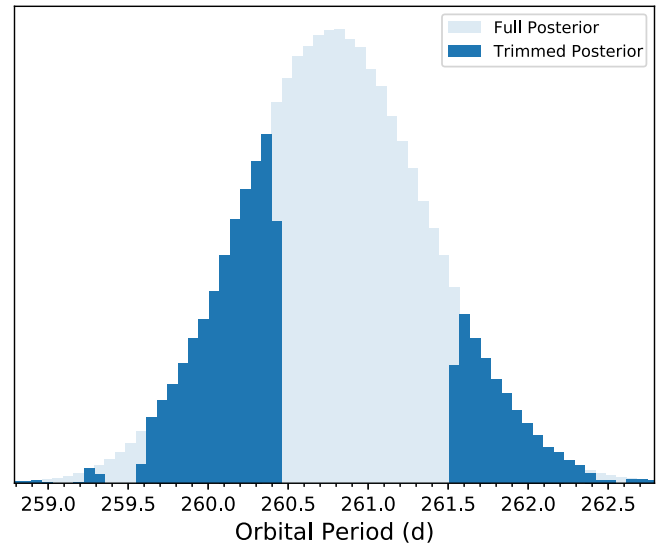


Figure 5. Orbital period posterior for TOI-2180 b. The light blue shows the full posterior, while the dark blue shows the region that is still allowed after the transit ephemeris refinement using ground-based photometry, which rules out the most likely orbital periods (around the mean and median) inferred from the comprehensive EXOFASTv2 analysis.

important. However, this metric can be recalculated for any future single-transit detection campaigns that yield nondetections or proposals to conduct such campaigns to compare strategies and assess effectiveness.

4.1. Prospects for Future Transit Detection

Despite the ephemeris refinement for TOI-2180 b conducted here, future characterization of this planet will be challenging until another transit is detected. The third transit of TOI-2180 b (assuming the TESS transit as the first) occurred sometime in 2021 mid-May and was not observed. The fourth transit is predicted to occur in late January or early 2022 February. Specifically, our predictions following the trimmed orbital period posterior are 19:19:30 UTC 2022 January 31 and 13:05:05 UTC 2022 February 5. The uncertainties on these predictions are asymmetric but roughly on the order of a day or less (1σ).

Fortunately, TESS is expected to reobserve TOI-2180 in Sector 48 of the extended mission beginning around 28 January 2022.⁶² We therefore predict that TESS will observe another transit of TOI-2180 b at that time. Barring data gaps, if another transit is not seen by TESS in Sector 48, then only a small (relatively unlikely) tail of the orbital period posterior distribution would be consistent with the original single transit and the RVs.

A second transit detection would drastically reduce the uncertainty on the orbital period and preserve the transit ephemeris for years into the future. However, some giant planets on 100–1000 day orbits are known to exhibit daylong timing variations from transit to transit (e.g., Wang et al. 2015). A third transit would need to be observed to explore the existence of transit timing variations (e.g., Dalba & Tamburo 2019).

⁶² According to the Web TESS Viewing Tool (<https://heasarc.gsfc.nasa.gov/cgi-bin/tess/webtess/wtv.py>) accessed 2021 September 4.

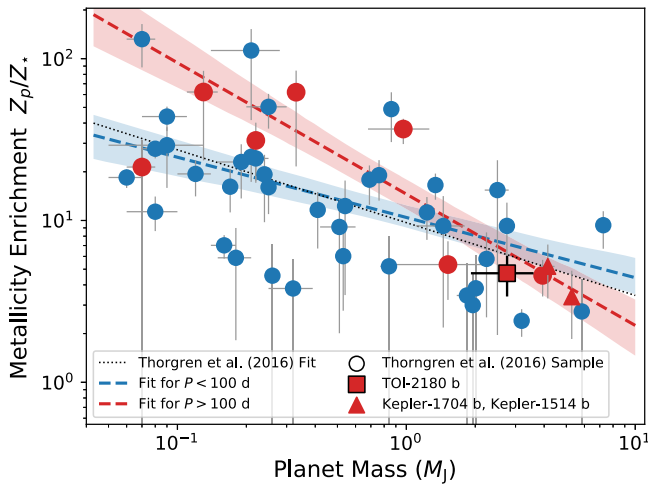


Figure 6. Giant planet mass–metallicity correlation shown with the Thorngren et al. (2016) sample (circles), TOI-2180 b (square), and two recently published Kepler long-period giant planets (triangles): Kepler-1514 b ($P \approx 218$ days) and Kepler-1704 b ($P \approx 989$ days). Blue and red indicate orbital periods below and above 100 days, respectively. The dashed lines and shaded 1σ regions indicate separate regressions to these two sets of planets. The slopes of these fits are discrepant to 2.6σ , hinting that the mass–metallicity correlation for giant planets may be dependent upon orbital properties.

5. Bulk Heavy-element Analysis

Object TOI-2180 b is one of a small but growing collection of valuable giant transiting exoplanets on \sim au-scale orbits with precisely measured masses and radii (e.g., Dubber et al. 2019; Dalba et al. 2021a, 2021b; Chachan et al. 2021). With these two properties, we can infer bulk heavy-element mass and metallicity relative to stellar to better understand their structure and formation history.

Following Thorngren & Fortney (2019), we generated one-dimensional spherically symmetric giant planet structure models with a rock/ice core; a convective envelope consisting of rock, ice, and H/He; and a radiative atmosphere interpolated from the Fortney et al. (2007) grid. Along with the mass, radius, and age for TOI-2180 b (drawn from the posteriors of the EXOFASTv2 fit), the models recovered the total mass of heavy elements and thereby bulk metallicity needed to explain the planet’s size. We find that the bulk metallicity for TOI-2180 b is $Z_p = 0.12 \pm 0.03$, which corresponds to $105 M_\oplus$ of heavy elements. We can approximate the stellar metallicity using the iron abundance following $Z_* = 0.142 \times 10^{[\text{Fe}/\text{H}]}$, which gives $Z_* = 0.0254 \pm 0.0033$. This sets the metal enrichment (Z_p/Z_*) at 4.7 ± 1.3 .

The metallicity enrichment of TOI-2180 b is consistent with the core accretion theory of giant planet formation (Pollack et al. 1996) with late-stage accretion of icy planetesimals, which can explain enrichment by a factor of a few to a dozen (e.g., Gautier et al. 2001; Mousis et al. 2009). An alternate theory to late-stage accretion—the mergers of planetary cores during the gas accretion phase (e.g., Ginzburg & Chiang 2020)—can explain enrichment factors between 1.5 and 10 for a $2.7 M_J$ planet, making it a viable formation pathway as well.

In Figure 6, we plot the mass and metal enrichment of TOI-2180 b relative to the Thorngren et al. (2016) sample of giant exoplanets. We also include two other recently published high-mass giant exoplanets on long-period orbits: Kepler-1514 b ($P \approx 218$ days; Dalba et al. 2021a) and Kepler-1704 b ($P \approx 989$ days; Dalba et al. 2021b). The metal enrichment of TOI-2180 b

relative to its host star is consistent with other giant planets with similar mass and falls near the best-fit line for all of the Thorngren et al. (2016) sample.

The Thorngren et al. (2016) exoplanets are plotted in Figure 6 as circles. The points are given different colors based on orbital period. The two Kepler planets are shown as triangles, and TOI-2180 b is shown as a square. Although each of these planets individually is fully consistent with the Thorngren et al. (2016) mass–metallicity correlation, there is possibly a subtle difference in the slope of the relation for the longer-period planets. For lower-mass planets, enrichment appears to be higher than average for the longer-period objects, and vice versa for the higher-mass planets, including TOI-2180 b.

We explored this possibility quantitatively by separating the planets in Figure 6 into short-period ($P < 100$ days) and long-period ($P \geq 100$ days) groups. The median orbital periods in the two groups were 10 and 223 days. Object TOI-2180 b and the Kepler planets are also given the corresponding $P > 100$ day color. Although 100 days is a somewhat arbitrary separation value, it possibly separates planets that experienced different formation histories. We conducted orthogonal distance regression fits, which include uncertainties on both the explanatory and response variables, to both sets of planet masses and metal enrichments in log space. The resulting power-law fits are drawn as dashed lines in Figure 6. The 1σ uncertainty regions are also shown. The fits for the short- and long-period planets are $(10.4 \pm 1.6) M^{(-0.372 \pm 0.084)}$ and $(14.6 \pm 2.9) M^{(-0.81 \pm 0.14)}$, respectively. The slopes in these fits are inconsistent at 2.6σ .

The mass–metallicity correlation derived for planets with orbital periods below 100 days is fully consistent with that measured by Thorngren et al. (2016). On the other hand, the small set of long-period planets that includes TOI-2180 b produces a notably steeper correlation. We refrain from placing too much emphasis on this finding owing to the small number of data points and moderate statistical significance. The addition of any number of additional long-period giant planets would be elucidating. If this trend is real, though, it suggests that the current orbital properties of giant planets trace different heavy-element accretion mechanisms, such as pebble or planetesimal (Hasegawa et al. 2018). A statistically robust analysis of the mass–metallicity correlation is warranted, but we leave such an analysis to future work.

For a solar system comparison, the Galileo Entry Probe measured volatile gases in Jupiter’s atmosphere and identified enrichment of 2–6 for several heavy elements and noble gases (Wong et al. 2004). More recently, the Juno spacecraft measured the equatorial water abundance on Jupiter to be one to five times the protosolar value (Li et al. 2020). The comparison between our enrichment measurement of TOI-2180 b and these measurements at Jupiter comes with caveats. For instance, the Jupiter enrichment is derived from its equatorial oxygen abundance, while the exoplanet enrichment is a model-dependent bulk value. The direct comparison of these two qualities may be problematic. However, the main point is that these values are all of a similar order of magnitude.

6. Analysis of RV Drift

We characterized the trend and curvature in TOI-2180’s RV time series using the technique described in Lubin et al. (2021). Because TOI-2180 is not in the Hipparcos catalog (ESA 1997),

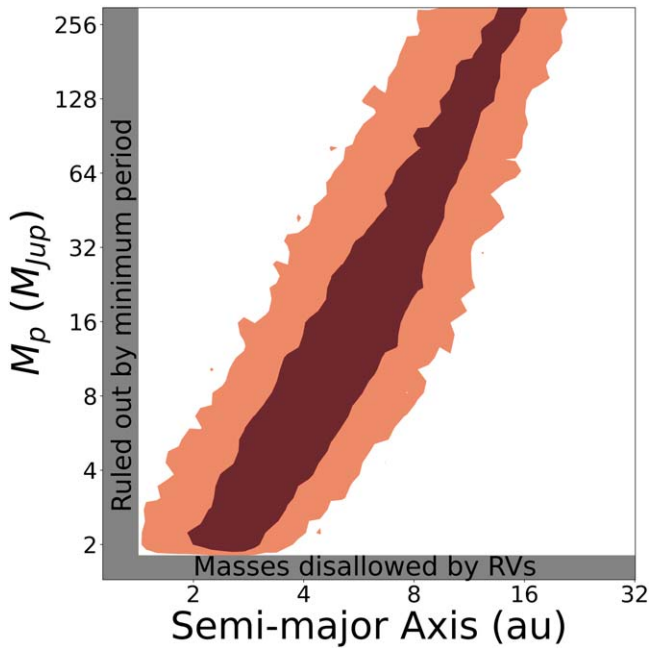


Figure 7. Set of (a, M_P) models consistent with the measured RV trend and curvature at the 1σ (dark) and 2σ (light) levels. We rule out semimajor axes corresponding to orbital periods shorter than the observing baseline, as well as companion masses too low to produce the minimum RV amplitude.

we could not calculate its astrometric acceleration using the Hipparcos–Gaia Catalog of Accelerations (Brandt 2018). Instead, we analyzed only the RV data, which leaves a degeneracy between companion mass and semimajor axis.

We sampled 10^8 synthetic companion models, each comprising a mass M_P , semimajor axis a , eccentricity e , inclination i , argument of periastron ω , and mean anomaly M . For each model companion, we calculated the trend $\langle \dot{\gamma} \rangle$ and curvature $\langle \ddot{\gamma} \rangle$ that such a companion would produce. We then calculated the model likelihood given the measured trend and curvature in Table 3 and marginalized over $\{e, i, \omega, M\}$ by binning the likelihoods in a – M_P space. Figure 7 shows the joint posterior distribution for TOI-2180’s companion.

If located within a few au, the object is likely to be planetary and more massive than $\sim 2 M_J$. Past roughly 8 au, however, the object transitions to the substellar regime. We truncate the upper mass boundary of Figure 7 at a few tenths of a solar mass, at which point we would have expected to detect such a companion in the speckle imaging (Section 2.2). For a $13 M_J$ object, if we extend the RV monitoring by an additional ~ 3.5 yr, we will have sampled between 25% and 100% of the full orbit by period. At that point, we should be more capable of distinguishing between planetary and nonplanetary scenarios.

7. Discussion

With an equilibrium temperature of 348 K (assuming a Jupiter-like Bond albedo; see Table 3), TOI-2180 b qualifies as a temperate Jupiter that occupies an interesting region of parameter space. It exists within 1–3 au, where the giant planet occurrence rate increases (e.g., Fernandes et al. 2019; Wittenmyer et al. 2020; Fulton et al. 2021), but it is not so close to its star that its orbit has been tidally circularized (e.g., following a high-eccentricity migration pathway). This means that its orbital properties may contain information about previous migration. Object TOI-2180 b is warmer than Jupiter

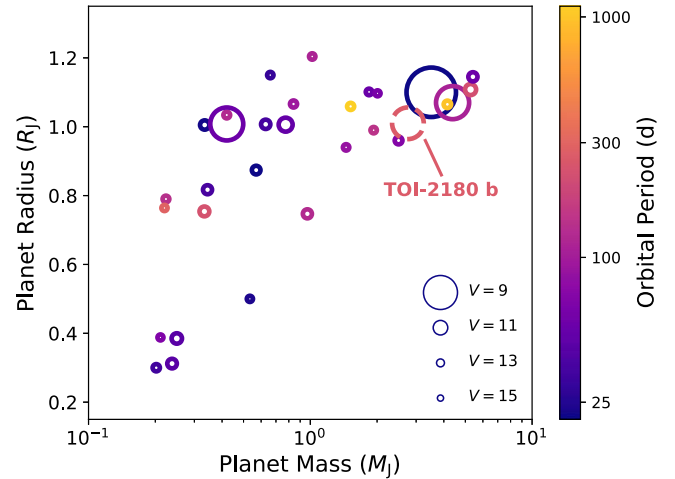


Figure 8. Subset of long-period ($P > 20$ days) giant ($M_P > 0.2 M_J$) exoplanets with measured mass and radii sized to show their hosts’ V -band magnitudes. Object TOI-2180 b is labeled and drawn with a dashed line. Of the four planets with the brightest host stars, TOI-2180 b has the longest period by far, demonstrating how it is a valuable extension of the parameter space of temperate Jupiters.

and Saturn, but it receives a weak enough irradiation to not be inflated. Planets like this are useful laboratories for models of interior and atmospheric structure and planet formation.

Object TOI-2180 b stands out among other transiting temperate Jupiters for two main reasons: its long orbital period and its host star’s favorable brightness. In Figure 8, we put TOI-2180 b in context with other giant planets ($M_P > 0.2 M_J$) with orbital periods greater than 20 days (to exclude hot Jupiters) with a measured mass and radius that did not have a controversial flag.⁶³ The Kepler mission has so far proven most successful at discovering planets in this region of parameter space (e.g., Wang et al. 2015; Foreman-Mackey et al. 2016; Uehara et al. 2016; Kawahara & Masuda 2019). As a result, many of the planets in Figure 8 are sufficiently faint that follow-up opportunities to further characterize their systems are very limited. TESS, however, is slowly beginning to populate the long-period giant planet parameter space with systems orbiting bright host stars that are more amenable to follow-up characterization (e.g., Eisner et al. 2020).

As a temperate giant planet, the atmosphere of TOI-2180 b represents a stepping-stone between well-characterized hot Jupiters and the cold solar system giant planets. At 348 K, we might expect to find nonequilibrium carbon chemistry that relies heavily on vertical transport (Fortney et al. 2020). Moreover, an atmospheric metallicity measurement of TOI-2180 b would be an ideal comparison to the now-known stellar and bulk planetary metallicity. Perhaps the atmospheric metallicity will be lower than the bulk value, since some amount of the heavy elements is likely sequestered into a core. However, evidence from solar system observations suggests that giant planets may instead have interior regions of inward-decreasing metallicity (e.g., Wahl et al. 2017; Guillot et al. 2018; Debras & Chabrier 2019). These theories could possibly be explored with transmission spectroscopy, which is suspected to probe CH_4 and the by-products of disequilibrium chemistry and photolysis in long-period giant planets (Dalba et al. 2015; Fortney et al. 2020). However, owing to its high surface gravity and an unfavorable planet–star radius ratio, TOI-2180 b is

⁶³ According to the NASA Exoplanet Archive, accessed 2021 September 5.

likely not amenable to transmission spectroscopy. The atmospheric scale height of TOI-2180 b is only ~ 23 km, which corresponds to a transit depth of a few parts per million (ppm) and a transmission spectroscopy metric of 7 (Kempton et al. 2018). Similarly, the near-infrared depth of the secondary eclipse is likely to be on the order of or less than 10 ppm (Table 3). Any future endeavor to identify favorable targets for temperate Jupiter atmospheric characterization should examine whether the brightness of TOI-2180 compensates for the difficulty introduced by its large stellar radius and the high surface gravity of TOI-2180 b.

Other avenues of follow-up characterization for the TOI-2180 system are more promising. Continued RV monitoring of TOI-2180 would eventually capture a sufficient fraction of the long-term acceleration to infer the properties of the outer companion. This RV trend could also be interpreted jointly with imaging and astrometric data to further constrain the outer object’s orbit and inclination (e.g., Crepp et al. 2012; Wittrock et al. 2016; Kane et al. 2019; Brandt et al. 2021; Dalba et al. 2021c). Be it a star or substellar object, it could have influenced the evolution and migration of TOI-2180 b, including eccentricity excitation through Kozai–Lidov oscillations (e.g., Wu & Murray 2003; Fabrycky & Tremaine 2007; Naoz et al. 2012). However, we need not invoke secular interactions (e.g., Wu & Lithwick 2011) or planet–planet scattering (e.g., Rasio & Ford 1996) to explain the moderate eccentricity ($e \approx 0.37$) of TOI-2180 b. Debras et al. (2021) argued that disk cavity migration could explain warm Jupiter eccentricity up to ~ 0.4 . Additional modeling of the formation and dynamical evolution of the objects in the TOI-2180 system with comparison to the bulk metallicity of TOI-2180 b would be illuminating.

The degeneracy between disk migration and secular interactions could possibly be broken with a measurement of the stellar obliquity via the Rossiter–McLaughlin (RM) effect (Rossiter 1924; McLaughlin 1924). Migration via interactions with a distant massive object would cause both orbits to be misaligned with the stellar spin. Alternatively, if it migrated in the disk, and the disk is assumed to have been aligned with the stellar equator, we would expect little obliquity. This assumption may be problematic, though, as disks can be tilted such that they yield misaligned planets under disk migration (e.g., Spalding & Batygin 2016). Nonetheless, the SpecMatch analysis of the TOI-2180 spectrum returned a low rotational velocity of $v \sin i = 2.2 \pm 1.0$ km s $^{-1}$. The largest possible amplitude of the RM effect would therefore be ~ 9 m s $^{-1}$ (Winn 2010), which is well within the capabilities of next-generation precise RV facilities such as MAROON-X (Seifahrt et al. 2018) or the Keck Planet Finder (Gibson et al. 2016). The RM effect would also be detectable from either Keck-HIRES or APF-Levy, which have average internal RV precisions of 1.2 and 3.6 m s $^{-1}$, respectively. Achieving the proper timing for such an experiment given the 24 hr transit is challenging, though, and may not be feasible for several years. The scientific benefit of an RM detection for this system, and for such a long-period planets in general, further motivates the need to refine the transit ephemeris.

Lastly, we briefly consider TOI-2180 b as a host for exomoons. The TESS transit offered no evidence to suggest that an exomoon is present, but the stellar brightness, long-period planetary orbit, and (possibly) gentle migration history raise the possibility of exomoon detection in this system. Object TOI-2180 is sufficiently bright that the precision of a

single-transit observation would likely reach the noise floors of NIRISS and NIRSpec (several tens of ppm; Greene et al. 2016; Batalha et al. 2017). A Ganymede-size moon would produce an ~ 5 ppm transit, which would not be detectable. Alternatively, an Earth-sized moon would yield an ~ 30 ppm occultation, which is more reasonable. As more transits of TOI-2180 b are observed by TESS or any other facility, we recommend that the community conduct photodynamical modeling to test for variations in transit timing and duration that might indicate the presence or lack of an exomoon (e.g., Kipping et al. 2012; Heller et al. 2014; Kipping 2021).

8. Summary

Single-transit events are the primary avenue to discovering exoplanets with orbital periods longer than approximately a month in TESS photometry. Here we describe the follow-up effort surrounding a 24 hr long single transit of TOI-2180 (Figure 1), a slightly evolved mid-G-type star, in Sector 19 data from TESS (Section 2.1). Citizen scientists identified the transit event shortly after the data became public, allowing a Doppler monitoring campaign with the APF telescope to begin immediately (Section 2.3). After nearly 2 yr of RV observations with the APF and Keck telescopes (Figure 3), we determined that TOI-2180 b—a $2.8 M_J$ giant planet on a 260.79 day eccentric (0.368) orbit—was the cause of the single-transit event (Section 3.1).

Object TOI-2180 b is a member of a rare but growing sample of valuable transiting giant exoplanets with orbital periods in the hundreds of days. We conduct a thorough comprehensive fit to the transit and RV data to infer the stellar and planetary properties of this system (Section 3.2). Our precise and regularly sampled RVs refine the ephemeris of TOI-2180 b, and we attempt to detect a second transit through 11 days of photometric observations with ground-based telescopes situated over three continents (Figure 9). Although we do not detect a transit in these data, we develop a straightforward method to combine the orbital period posterior from the fit to the single transit and RVs with the extensive collection of ground-based data sets (Section 4). This analysis substantially refines the orbital period of TOI-2180 b by eliminating a substantial fraction of the most likely posterior solutions (Figure 5), leaving the prediction that TESS will likely detect the transit of TOI-2180 b in 2022 January or February (Section 4.1).

With a measured mass and radius for TOI-2180 b, we infer the bulk heavy-element content and metallicity relative to stellar from interior structure models (Section 5). It is likely that TOI-2180 b has over $100 M_{\oplus}$ of heavy elements in its envelope and interior and is enriched relative to its host star by a factor of 4.7 ± 1.3 . We place TOI-2180 b in the context of the mass–metallicity correlation for giant planets in Figure 6. Along with a few other recently characterized exoplanets on several hundred day orbital periods, TOI-2180 b suggests at 2.6σ confidence that the relation between metal enrichment (relative to stellar) and mass for giant planets is dependent on orbital properties. We leave further analysis of this possibility to future work.

Lastly, we place the discovery of TOI-2180 b in the context of other temperate giant planets with known mass and radius (Section 7, Figure 8). It is a poor candidate for transmission spectroscopy owing to its high surface gravity and the $1.6 R_{\odot}$ radius of its host star. Still, this system is a promising target for

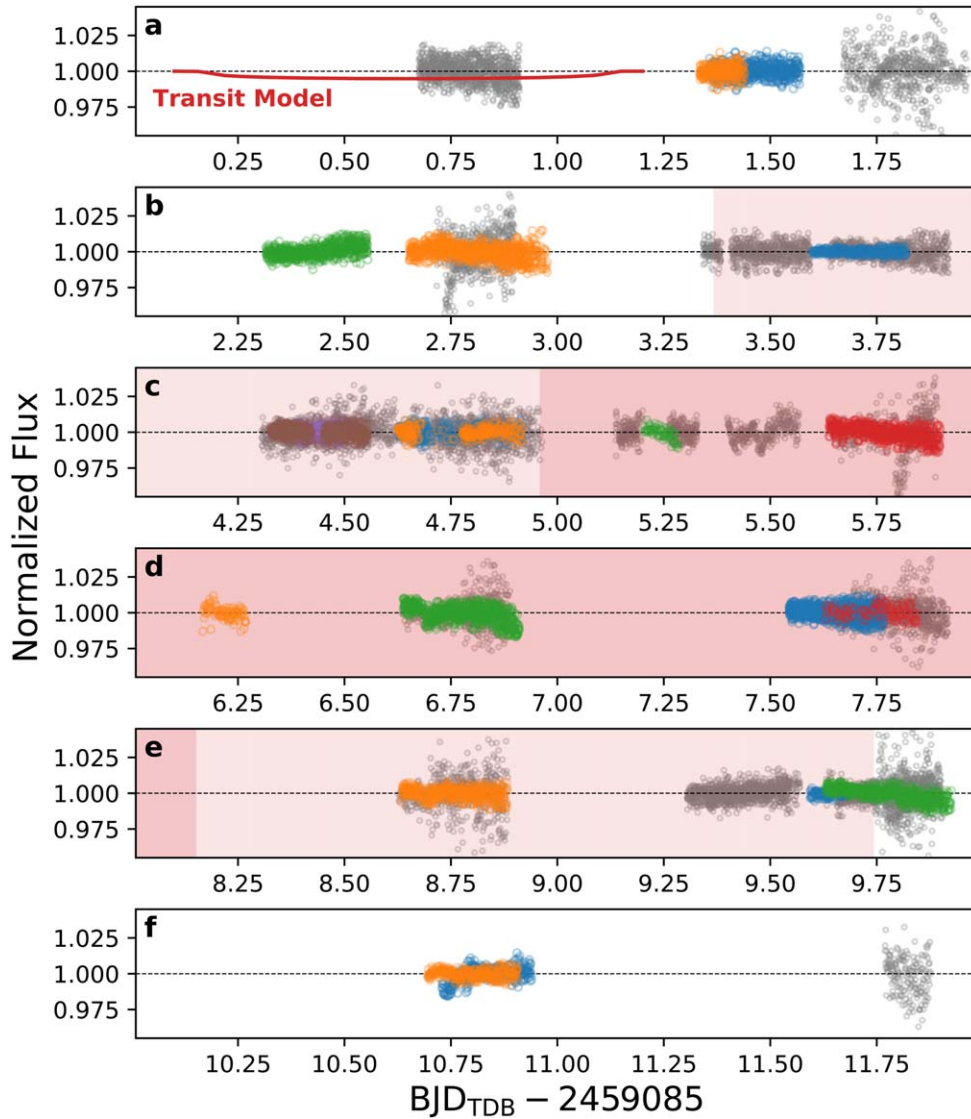


Figure 9. All ground-based data acquired in the transit ephemeris refinement effort for TOI-2180 b. These data have not been detrended against airmass variations. The transit model is shown in panel (a) for comparison only (i.e., we are not suggesting that occurred at that time). The light and dark shaded regions denote the 2σ and 1σ transit windows, respectively, calculated from the final ephemeris in Table 3. Data sets plotted with a color were used to refine the orbital period of TOI-2180 b, whereas those in gray are shown only for completeness. These data are summarized in Table 4 and will be made available upon request.

continued RV monitoring and stellar obliquity measurement to test theories of how giant planets migrate within the occurrence rate increase near 1 au but not so close as to become hot Jupiters. Object TOI-2180 b also remains an excellent candidate for exomoon investigations, since the host star brightness ($V=9.2; J=8.0$) makes it amenable to incredibly precise space-based photometry in the future.

The authors recognize and acknowledge the cultural role and reverence that the summit of Maunakea has within the indigenous Hawaiian community. We are deeply grateful to have the opportunity to conduct observations from this mountain.

The authors would like to thank the anonymous referee for helpful comments that improved this paper. We also thank Jack Lissauer for interesting conversations about giant planets that guided some of our analysis. We thank Ken and Gloria Levy, who supported the construction of the Levy Spectrometer on the Automated Planet Finder. We thank the

University of California and Google for supporting Lick Observatory and the UCO staff for their dedicated work scheduling and operating the telescopes of Lick Observatory. Some of the data presented herein were obtained at the W. M. Keck Observatory, which is operated as a scientific partnership among the California Institute of Technology, the University of California, and NASA. The Observatory was made possible by the generous financial support of the W. M. Keck Foundation.

This paper includes data collected by the TESS mission. Funding for the TESS mission is provided by NASA’s Science Mission Directorate. We acknowledge the use of public TESS data from pipelines at the TESS Science Office and the TESS Science Processing Operations Center. Resources supporting this work were provided by the NASA High-End Computing (HEC) Program through the NASA Advanced Supercomputing (NAS) Division at Ames Research Center for the production of the SPOC data products. This research has made use of the NASA Exoplanet Archive, which is operated by the California

Institute of Technology, under contract with the National Aeronautics and Space Administration under the Exoplanet Exploration Program. This research has made use of the Exoplanet Follow-up Observation Program website, which is operated by the California Institute of Technology, under contract with the National Aeronautics and Space Administration under the Exoplanet Exploration Program. This paper includes data collected with the TESS mission, obtained from the MAST data archive at the Space Telescope Science Institute (STScI). The STScI is operated by the Association of Universities for Research in Astronomy, Inc., under NASA contract NAS 5-26555. We acknowledge the use of public TESS data from pipelines at the TESS Science Office and the TESS Science Processing Operations Center. This work makes use of observations from the LCOGT network. Part of the LCOGT telescope time was granted by NOIRLab through the Mid-Scale Innovations Program (MSIP). MSIP is funded by NSF.

P.D. is supported by a National Science Foundation (NSF) Astronomy and Astrophysics Postdoctoral Fellowship under award AST-1903811. E.A.P. acknowledges the support of the Alfred P. Sloan Foundation. L.M.W. is supported by the Beatrice Watson Parrent Fellowship and NASA ADAP grant 80NSSC19K0597. A.C. is supported by the NSF Graduate Research Fellowship, grant No. DGE 1842402. D.H. acknowledges support from the Alfred P. Sloan Foundation, the National Aeronautics and Space Administration (80NSSC21K0652), and the National Science Foundation (AST-1717000). I.J.M.C. acknowledges support from the NSF through grant AST-1824644. R.A.R. is supported by the NSF Graduate Research Fellowship, grant No. DGE 1745301. C.D.D. acknowledges the support of the Hellman Family Faculty Fund, the Alfred P. Sloan Foundation, the David & Lucile Packard Foundation, and the National Aeronautics and Space Administration via the TESS Guest Investigator Program (80NSSC18K1583). J.M.A.M. is supported by the NSF Graduate Research Fellowship, grant No. DGE-1842400. J.M.A.M. also acknowledges the LSSTC Data Science Fellowship Program, which is funded by LSSTC, NSF Cybertraining grant No. 1829740, the Brinson Foundation, and the Moore Foundation; his participation in the program has benefited this work. T.F. acknowledges support from the University of California President’s Postdoctoral Fellowship Program. N.E. acknowledges support from the UK Science and Technology Facilities Council (STFC) under grant code ST/R505006/1. D.D. acknowledges support from TESS Guest Investigator Program grant 80NSSC19K1727 and NASA Exoplanet Research Program grant 18-2XRP18_2-0136. M.R. is supported by the National Science Foundation Graduate Research Fellowship Program under grant No. DGE-1752134.

P.D. thanks the Walmart of Yucca Valley, California, for frequent and prolonged use of its wireless internet to upload hundreds of gigabytes of data.

Facilities: Keck:I (HIRES), Automated Planet Finder (Levy), TESS, Gemini:Gillett (‘Alopeke), LCOGT.

Software: batman (Kreidberg 2015), EXOFASTv2 (Eastman et al. 2013; Eastman 2017; Eastman et al. 2019), lightkurve (Lightkurve Collaboration et al. 2018), RadVel (Fulton et al. 2018), SpecMatch (Petigura 2015; Petigura et al. 2017), AstroImageJ (Collins et al. 2017), LcTools (Schmitt et al. 2019).

Appendix Ground-based Telescope Light Curves of TOI-2180

In the following sections, we briefly describe each telescope that contributed to the ground-based observing campaign. Additional information summarizing the campaign is provided in Table 4.

A.1. Maury Lewin Astronomical Observatory

The Maury Lewin Astronomical Observatory (MLO) consists of a 0.356 m Schmidt–Cassegrain telescope located near Glendora, California, USA. The MLO has an SBIG STF8300M detector with a $23' \times 17'$ field of view. Observations of TOI-2180 were conducted in the *B* and *I* bands with various exposure times between 15 and 50 s. The data were reduced and analyzed with AstroImageJ (AIJ) following the standard differential aperture photometry protocol described by Collins et al. (2017).

A.2. Kotizarovci Observatory

Kotizarovci Observatory (SCT) consists of a 0.3 m Schmidt–Cassegrain telescope located near Viskovo, Croatia. The SCT has an SBIG ST7XME detector with a $15'3 \times 10'2$ field of view. Observations of TOI-2180 were conducted in a TESS-like filter with 20 s exposure times. The data were reduced and analyzed with AIJ following the standard differential aperture photometry protocol described by Collins et al. (2017).

A.3. Grand-Pra Observatory

Grand-Pra Observatory (RCO) consists of a 0.4 m Ritchey–Chretien telescope located near Sion, Valais, Switzerland. The RCO has a ProLine FLI 4710 detector with a $12'9 \times 12'55$ field of view. Observations of TOI-2180 were conducted in the z_s filter with 15 s exposure times. The data were reduced and analyzed with AIJ following the standard differential aperture photometry protocol described by Collins et al. (2017).

A.4. Boyce-Astro Research Observatory

The Boyce-Astro Research Observatory (BARO) consists of a 0.43 m Corrected Dall–Kirkham telescope located near San Diego, California, USA. BARO has a ProLine FLI 4710 detector with a $15'6$ square field of view. Observations of TOI-2180 were conducted in the *i'* filter with 3 s exposure times. The data were reduced and analyzed with AIJ following the standard differential aperture photometry protocol described by Collins et al. (2017).

A.5. LCOGT-Haleakalā Observatory

The Las Cumbres Observatory Global Telescope Network (LCOGT; Brown et al. 2013) hosts a 0.4 m Ritchey–Chretien Cassegrain telescope on Mt. Haleakalā in Maui, Hawai‘i, USA (LCOGT-HAL). The LCOGT-HAL has an SBIG STX6303 detector with a $29'2 \times 19'5$ field of view. Observations of TOI-2180 were conducted with the *B*, z_s , and *i'* filters with 30, 60, and 30 s exposure times, respectively. The data were reduced and analyzed with AIJ following the standard differential aperture photometry protocol described by Collins et al. (2017).

A.6. LCOGT-McDonald Observatory

The LCOGT hosts a 1.0 m Ritchey–Chretien Cassegrain telescope at McDonald Observatory near Fort Davis, Texas, USA (LCOGT-McD). The LCOGT-McD has a Sinistro detector with a 26'5 square field of view. Observations of TOI-2180 were conducted with the z_s filter with 20 s exposure times. The data were reduced and analyzed with AIJ following the standard differential aperture photometry protocol described by Collins et al. (2017).

A.7. Wendelstein Observatory

Wendelstein Observatory (W43) consists of a 0.43 m Corrected Dall–Kirkham telescope located near Bayrischzell, Germany. The W43 has an SBIG STX-16803 detector with a 45' square field of view. Observations of TOI-2180 were conducted in the i' filter with 5 s exposure times. The data were reduced and analyzed with a custom differential aperture photometry pipeline that maximizes light-curve precision by using multiple reference stars and testing various aperture sizes (Dalba & Muirhead 2016; Dalba et al. 2017).

A.8. Saint-Pierre-du-Mont Observatory

Saint-Pierre-du-Mont Observatory (OPM) consists of a 0.2 m Ritchey–Chretien telescope located near Saint-Pierre-du-Mont, France. The OPM has an Atik 383 L+ detector with a 38' \times 29' field of view. Observations of TOI-2180 were conducted in the I band with 25 or 40 s exposure times. The data were reduced and analyzed with AIJ following the standard differential aperture photometry protocol described by Collins et al. (2017).

A.9. LCOGT-Teide Observatory

The LCOGT hosts a 0.4 m Ritchey–Chretien Cassegrain telescope at Teide Observatory in Tenerife, Spain (LCOGT-TFN). The LCOGT-TFN has an SBIG STX6303 detector with a 29'2 \times 19'5 field of view. Observations of TOI-2180 were conducted with the i' filter with 30 s exposure times. The data were reduced and analyzed with AIJ following the standard differential aperture photometry protocol described by Collins et al. (2017).

A.10. Dragonfly Telephoto Array

The Dragonfly Telephoto Array (DRA), housed at the New Mexico Skies telescope hosting facility, is a remote telescope consisting of an array of small telephoto lenses roughly equivalent to a 1.0 m refractor (Danieli et al. 2020). The site is located near Mayhill, New Mexico, USA. The DRA has an SBIG STF8300M detector with a 156' \times 114' field of view. Simultaneous observations of TOI-2180 were conducted in the g' and r' bands with 15 s exposure times. The data were reduced and analyzed with a custom differential aperture photometry pipeline designed for multi-image processing and analysis.

A.11. eVscope Portable Observatories (eV-A, eV-B)

Object TOI-2180 was observed with two Unistellar eVscope telescopes positioned near Joshua Tree, California, USA. The eVscope is a digital, Newtonian-like 0.114 m telescope that contains a CMOS low-light IMX224 detector with a 37' \times 28'

field of view (Marchis et al. 2020). Both eVscopes observed TOI-2180 without a filter (i.e., clear) and with 3.975 s exposures that were subsequently stacked by a factor of 30. The stacked images were analyzed with a custom differential aperture photometry pipeline that maximizes light-curve precision by using multiple reference stars and testing various aperture sizes (Dalba & Muirhead 2016; Dalba et al. 2017).

A.12. Indian Astronomical Observatory

The Indian Astronomical Observatory hosts the 2.0 m Himalayan Chandra Telescope (HCT) near Ladakh, India. The HCT has an E2V detector with a 30' square field of view. Observations of TOI-2180 were conducted in the R band with 15 s exposure times. The data were reduced and analyzed with a custom differential aperture photometry pipeline that maximizes light-curve precision by using multiple reference stars and testing various aperture sizes (Dalba & Muirhead 2016; Dalba et al. 2017).

A.13. Vainu Bappu Observatory

The Vainu Bappu Observatory hosts the 1.3 m J. C. Bhattacharyya Telescope (JCB) near Tamil Nadu, India. The JCB has a UKATC detector with a 20' \times 10' field of view. Observations of TOI-2180 were conducted in the R band with 30 or 50 s exposure times. The data were reduced and analyzed with a custom differential aperture photometry pipeline that maximizes light-curve precision by using multiple reference stars and testing various aperture sizes (Dalba & Muirhead 2016; Dalba et al. 2017).

A.14. Acton Sky Portal

The Acton Sky Portal (ASP) consists of a 0.36 m Schmidt–Cassegrain telescope located near Acton, Massachusetts, USA. The ASP has an SBIG ST8-XME detector with a 24'2 \times 16'2 field of view. Observations of TOI-2180 were conducted in the r' band with 10 s exposure times. The data were reduced and analyzed with AIJ following the standard differential aperture photometry protocol described by Collins et al. (2017).


ORCID iDs

Paul A. Dalba  <https://orcid.org/0000-0002-4297-5506>
 Stephen R. Kane  <https://orcid.org/0000-0002-7084-0529>
 Diana Dragomir  <https://orcid.org/0000-0003-2313-467X>
 Steven Villanueva, Jr.  <https://orcid.org/0000-0001-6213-8804>
 Karen A. Collins  <https://orcid.org/0000-0001-6588-9574>
 Thomas Lee Jacobs  <https://orcid.org/0000-0003-3988-3245>
 Daryll M. LaCourse  <https://orcid.org/0000-0002-8527-2114>
 Martti H. Kristiansen  <https://orcid.org/0000-0002-2607-138X>
 Hans M. Schwengeler  <https://orcid.org/0000-0002-1637-2189>
 Andrew Vanderburg  <https://orcid.org/0000-0001-7246-5438>
 Benjamin Fulton  <https://orcid.org/0000-0003-3504-5316>
 Howard Isaacson  <https://orcid.org/0000-0002-0531-1073>
 Judah Van Zandt  <https://orcid.org/0000-0002-4290-6826>
 Andrew W. Howard  <https://orcid.org/0000-0001-8638-0320>

Daniel P. Thorngren  <https://orcid.org/0000-0002-5113-8558>

Steve B. Howell  <https://orcid.org/0000-0002-2532-2853>

Natalie M. Batalha  <https://orcid.org/0000-0002-7030-9519>

Ashley Chontos  <https://orcid.org/0000-0003-1125-2564>

Courtney D. Dressing  <https://orcid.org/0000-0001-8189-0233>


Daniel Huber  <https://orcid.org/0000-0001-8832-4488>

Erik A. Petigura  <https://orcid.org/0000-0003-0967-2893>

Paul Robertson  <https://orcid.org/0000-0003-0149-9678>

Arpita Roy  <https://orcid.org/0000-0001-8127-5775>

Lauren M. Weiss  <https://orcid.org/0000-0002-3725-3058>

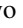
Aida Behmard  <https://orcid.org/0000-0003-0012-9093>

Corey Beard  <https://orcid.org/0000-0001-7708-2364>

Steven Giacalone  <https://orcid.org/0000-0002-8965-3969>

Michelle L. Hill  <https://orcid.org/0000-0002-0139-4756>

Jack Lubin  <https://orcid.org/0000-0001-8342-7736>

Andrew W. Mayo  <https://orcid.org/0000-0002-7216-2135>

Teo Močnik  <https://orcid.org/0000-0003-4603-556X>

Joseph M. Akana Murphy  <https://orcid.org/0000-0001-8898-8284>

Malena Rice  <https://orcid.org/0000-0002-7670-670X>

Lee J. Rosenthal  <https://orcid.org/0000-0001-8391-5182>

Ryan A. Rubenzahl  <https://orcid.org/0000-0003-3856-3143>


Nicholas Scarsdale  <https://orcid.org/0000-0003-3623-7280>


Thomas M. Esposito  <https://orcid.org/0000-0002-0792-3719>

Christopher R. Mann  <https://orcid.org/0000-0002-9312-0073>

Franck Marchis  <https://orcid.org/0000-0001-7016-7277>

Richard P. Schwarz  <https://orcid.org/0000-0001-8227-1020>


Nora L. Eisner  <https://orcid.org/0000-0002-9138-9028>

Tara Fetherolf  <https://orcid.org/0000-0002-3551-279X>


Zhexing Li  <https://orcid.org/0000-0002-4860-7667>


Xinyu Yao  <https://orcid.org/0000-0003-4554-5592>

Joshua Pepper  <https://orcid.org/0000-0002-3827-8417>

George R. Ricker  <https://orcid.org/0000-0003-2058-6662>

Roland Vanderspek  <https://orcid.org/0000-0001-6763-6562>

David W. Latham  <https://orcid.org/0000-0001-9911-7388>

Joshua N. Winn  <https://orcid.org/0000-0002-4265-047X>


Jon M. Jenkins  <https://orcid.org/0000-0002-4715-9460>

Christopher J. Burke  <https://orcid.org/0000-0002-7754-9486>

Jason D. Eastman  <https://orcid.org/0000-0003-3773-5142>

Michael B. Lund  <https://orcid.org/0000-0003-2527-1598>

Pamela Rowden  <https://orcid.org/0000-0002-4829-7101>

Eric B. Ting  <https://orcid.org/0000-0002-8219-9505>

References

- Akinsanmi, B., Oshagh, M., Santos, N. C., & Barros, S. C. C. 2018, *A&A*, **609**, A21
- Barnes, J. W., & Fortney, J. J. 2004, *ApJ*, **616**, 1193
- Batalha, N. E., Mandell, A., Pontoppidan, K., et al. 2017, *PASP*, **129**, 064501
- Beichman, C., Livingston, J., Werner, M., et al. 2016, *ApJ*, **822**, 39
- Belokurov, V., Penoyre, Z., Oh, S., et al. 2020, *MNRAS*, **496**, 1922
- Borucki, W. J., Koch, D., Basri, G., et al. 2010, *Science*, **327**, 977
- Brandt, T. D. 2018, *ApJS*, **239**, 31
- Brandt, T. D., Dupuy, T. J., Li, Y., et al. 2021, *AJ*, **162**, 186
- Brown, T. M., Baliber, N., Bianco, F. B., et al. 2013, *PASP*, **125**, 1031
- Burt, J., Holden, B., Hanson, R., et al. 2015, *JATIS*, **1**, 044003
- Butler, R. P., Marcy, G. W., Williams, E., et al. 1996, *PASP*, **108**, 500
- Chachan, Y., Dalba, P. A., & Knutson, H. A. 2021, arXiv:2112.00747
- Chontos, A., Akana Murphy, J. M., MacDougall, M. G., et al. 2021, arXiv:2106.06156
- Claret, A., & Bloemen, S. 2011, *A&A*, **529**, A75

- Collins, K. A., Kielkopf, J. F., Stassun, K. G., & Hessman, F. V. 2017, *AJ*, **153**, 77
- Cooke, B. F., Pollacco, D., Anderson, D. R., et al. 2021, *MNRAS*, **500**, 5088
- Crepp, J. R., Johnson, J. A., Howard, A. W., et al. 2012, *ApJ*, **761**, 39
- Cutri, R. M., Skrutskie, M. F., van Dyk, S., et al. 2003, *yCat*, **II/246**
- Cutri, R. M., Wright, E. L., Conrow, T., et al. 2014, *yCat*, **II/328**
- Dai, F., Roy, A., Fulton, B., et al. 2020, *AJ*, **160**, 193
- Dalba, P. A., Fulton, B., Isaacson, H., Kane, S. R., & Howard, A. W. 2020a, *AJ*, **160**, 149
- Dalba, P. A., Gupta, A. F., Rodriguez, J. E., et al. 2020b, *AJ*, **159**, 241
- Dalba, P. A., Kane, S. R., Howell, S. B., et al. 2021c, *AJ*, **161**, 123
- Dalba, P. A., Kane, S. R., Isaacson, H., et al. 2021a, *AJ*, **161**, 103
- Dalba, P. A., Kane, S. R., Li, Z., et al. 2021b, *AJ*, **162**, 154
- Dalba, P. A., & Muirhead, P. S. 2016, *ApJL*, **826**, L7
- Dalba, P. A., Muirhead, P. S., Croll, B., & Kempton, E. M.-R. 2017, *AJ*, **153**, 59
- Dalba, P. A., Muirhead, P. S., Fortney, J. J., et al. 2015, *ApJ*, **814**, 154
- Dalba, P. A., & Tamburo, P. 2019, *ApJL*, **873**, L17
- Danieli, S., Lokhorst, D., Zhang, J., et al. 2020, *ApJ*, **894**, 119
- Debras, F., Baruteau, C., & Donati, J.-F. 2021, *MNRAS*, **500**, 1621
- Debras, F., & Chabrier, G. 2019, *ApJ*, **872**, 100
- Diaz, M. R., Jenkins, J. S., Feng, F., et al. 2020, *MNRAS*, **496**, 4330
- Dotter, A. 2016, *ApJS*, **222**, 8
- Dubber, S. C., Mortier, A., Rice, K., et al. 2019, *MNRAS*, **490**, 5103
- Eastman, J. 2017, EXOFASTv2: Generalized Publication-quality Exoplanet Modeling Code, v2, Astrophysics Source Code Library, ascl:1710.003
- Eastman, J., Gaudi, B. S., & Agol, E. 2013, *PASP*, **125**, 83
- Eastman, J. D., Rodriguez, J. E., Agol, E., et al. 2019, arXiv:1907.09480
- Eisner, N. L., Barragán, O., Aigrain, S., et al. 2020, *MNRAS*, **494**, 750
- Eisner, N. L., Barragán, O., Lintott, C., et al. 2021, *MNRAS*, **501**, 4669
- ESA 1997, VizieR On-line Data Catalog, **1/239**
- Fabrycky, D., & Tremaine, S. 2007, *ApJ*, **669**, 1298
- Fernandes, R. B., Mulders, G. D., Pascucci, I., Mordasini, C., & Emsenhuber, A. 2019, *ApJ*, **874**, 81
- Ford, E. B. 2006, *ApJ*, **642**, 505
- Foreman-Mackey, D., Morton, T. D., Hogg, D. W., Agol, E., & Schölkopf, B. 2016, *AJ*, **152**, 206
- Fortney, J. J., Marley, M. S., & Barnes, J. W. 2007, *ApJ*, **659**, 1661
- Fortney, J. J., Visscher, C., Marley, M. S., et al. 2020, *AJ*, **160**, 288
- Fulton, B. J., Petigura, E. A., Blunt, S., & Sinukoff, E. 2018, *PASP*, **130**, 044504
- Fulton, B. J., Rosenthal, L. J., Hirsch, L. A., et al. 2021, *ApJS*, **255**, 14
- Fulton, B. J., Weiss, L. M., Sinukoff, E., et al. 2015, *ApJ*, **805**, 175
- Gaia Collaboration, Brown, A. G. A., Vallenari, A., et al. 2018, *A&A*, **616**, A1
- Gaia Collaboration, Brown, A. G. A., Vallenari, A., et al. 2021, *A&A*, **649**, A1
- Gautier, D., Hersant, F., Mousis, O., & Lunine, J. I. 2001, *ApJL*, **550**, L227
- Gelman, A., & Rubin, D. B. 1992, *StatSci*, **7**, 457
- Gibson, S. R., Howard, A. W., Marcy, G. W., et al. 2016, *Proc. SPIE*, **9908**, 990870
- Ginzburg, S., & Chiang, E. 2020, *MNRAS*, **498**, 680
- Greene, T. P., Line, M. R., Montero, C., et al. 2016, *ApJ*, **817**, 17
- Guerrero, N. M., Seager, S., Huang, C. X., et al. 2021, *ApJS*, **254**, 39
- Guillot, T., Miguel, Y., Militzer, B., et al. 2018, *Natur*, **555**, 227
- Guillot, T., Santos, N. C., Pont, F., et al. 2006, *A&A*, **453**, L21
- Hasegawa, Y., Bryden, G., Ikoma, M., Vasisht, G., & Swain, M. 2018, *ApJ*, **865**, 32
- Heller, R., Williams, D., Kipping, D., et al. 2014, *AsBio*, **14**, 798
- Herman, M. K., Zhu, W., & Wu, Y. 2019, *AJ*, **157**, 248
- Howard, A. W., Johnson, J. A., Marcy, G. W., et al. 2010, *ApJ*, **721**, 1467
- Howell, S. B., Everett, M. E., Sherry, W., Horch, E., & Ciardi, D. R. 2011, *AJ*, **142**, 19
- Isaacson, H., & Fischer, D. 2010, *ApJ*, **725**, 875
- Jenkins, J. M., Twicken, J. D., McCauliff, S., et al. 2016, *Proc. SPIE*, **9913**, 99133E
- Kane, S. R. 2007, *MNRAS*, **380**, 1488
- Kane, S. R., Ciardi, D. R., Gelino, D. M., & von Braun, K. 2012, *MNRAS*, **425**, 757
- Kane, S. R., Dalba, P. A., Li, Z., et al. 2019, *AJ*, **157**, 252
- Kass, R. E., & Raftery, A. E. 1995, *J. Am. Stat. Assoc.*, **90**, 773
- Kawahara, H., & Masuda, K. 2019, *AJ*, **157**, 218
- Kempton, E. M. R., Bean, J. L., Louie, D. R., et al. 2018, *PASP*, **130**, 114401
- Kipping, D. 2021, *MNRAS*, **500**, 1851
- Kipping, D. M., Bakos, G. Á., Buchhave, L., Nesvorný, D., & Schmitt, A. 2012, *ApJ*, **750**, 115
- Kreidberg, L. 2015, *PASP*, **127**, 1161
- LaCourse, D. M., & Jacobs, T. L. 2018, *RNAAS*, **2**, 28

- Li, C., Ingersoll, A., Bolton, S., et al. 2020, *NatAs*, **4**, 609
- Lightkurve Collaboration, Cardoso, J. V. d. M., Hedges, C., et al. 2018, Lightkurve: Kepler and TESS time series analysis in Python, 1.11, Astrophysics Source Code Library, ascl:1812.013
- Lindgren, L., Klioner, S. A., Hernández, J., et al. 2021, *A&A*, **649**, A2
- Lubin, J., Van Zandt, J., Holcomb, R., et al. 2021, arXiv:2108.02208
- Marchis, F., Malvache, A., Marfisi, L., Borot, A., & Arbouch, E. 2020, *AcAau*, **166**, 23
- Mayor, M., Marmier, M., Lovis, C., et al. 2011, arXiv:1109.2497
- McLaughlin, D. B. 1924, *ApJ*, **60**, 22
- Miller, N., & Fortney, J. J. 2011, *ApJL*, **736**, L29
- Mordasini, C., Klahr, H., Alibert, Y., Miller, N., & Henning, T. 2014, *A&A*, **566**, A141
- Mousis, O., Marboeuf, U., Lunine, J. I., et al. 2009, *ApJ*, **696**, 1348
- Naoz, S., Farr, W. M., & Rasio, F. A. 2012, *ApJL*, **754**, L36
- Osborn, H. P., Armstrong, D. J., Brown, D. J. A., et al. 2016, *MNRAS*, **457**, 2273
- Petigura, E. A. 2015, PhD thesis, Univ. of California, Berkeley
- Petigura, E. A., Howard, A. W., Marcy, G. W., et al. 2017, *AJ*, **154**, 107
- Pollack, J. B., Hubickyj, O., Bodenheimer, P., et al. 1996, *Icar*, **124**, 62
- Radovan, M. V., Cabak, G. F., Laiterman, L. H., Lockwood, C. T., & Vogt, S. S. 2010, *Proc. SPIE*, **7735**, 77354K
- Radovan, M. V., Lanclos, K., Holden, B. P., et al. 2014, *Proc. SPIE*, **9145**, 91452B
- Rasio, F. A., & Ford, E. B. 1996, *Science*, **274**, 954
- Ricker, G. R., Winn, J. N., Vanderspek, R., et al. 2015, *JATIS*, **1**, 014003
- Rossiter, R. A. 1924, *ApJ*, **60**, 15
- Rubenzahl, R. A., Dai, F., Howard, A. W., et al. 2021, *AJ*, **161**, 119
- Santerne, A., Hébrard, G., Deleuil, M., et al. 2014, *A&A*, **571**, A37
- Santerne, A., Malavolta, L., Kosiarek, M. R., et al. 2019, arXiv:1911.07355
- Schlafly, E. F., & Finkbeiner, D. P. 2011, *ApJ*, **737**, 103
- Schmitt, A. R., Hartman, J. D., & Kipping, D. M. 2019, arXiv:1910.08034
- Schwarz, G. 1978, *AnSta*, **6**, 461
- Seager, S., & Hui, L. 2002, *ApJ*, **574**, 1004
- Seifahrt, A., Stürmer, J., Bean, J. L., & Schwab, C. 2018, *Proc. SPIE*, **10702**, 107026D
- Shibata, S., Helled, R., & Ikoma, M. 2020, *A&A*, **633**, A33
- Smith, J. C., Stumpe, M. C., Van Cleve, J. E., et al. 2012, *PASP*, **124**, 1000
- Spalding, C., & Batygin, K. 2016, *ApJ*, **830**, 5
- Stassun, K. G., Oelkers, R. J., Paegert, M., et al. 2019, *AJ*, **158**, 138
- Stumpe, M. C., Smith, J. C., Catanzarite, J. H., et al. 2014, *PASP*, **126**, 100
- Stumpe, M. C., Smith, J. C., Van Cleve, J. E., et al. 2012, *PASP*, **124**, 985
- Tayar, J., Claytor, Z. R., Huber, D., & van Saders, J. 2020, arXiv:2012.07957
- Teske, J. K., Thorngren, D., Fortney, J. J., Hinkel, N., & Brewer, J. M. 2019, *AJ*, **158**, 239
- Thompson, S. E., Coughlin, J. L., Hoffman, K., et al. 2018, *ApJS*, **235**, 38
- Thorngren, D., & Fortney, J. J. 2019, *ApJL*, **874**, L31
- Thorngren, D. P., Fortney, J. J., Murray-Clay, R. A., & Lopez, E. D. 2016, *ApJ*, **831**, 64
- Uehara, S., Kawahara, H., Masuda, K., Yamada, S., & Aizawa, M. 2016, *ApJ*, **822**, 2
- Villanueva, S. J., Dragomir, D., & Gaudi, B. S. 2019, *AJ*, **157**, 84
- Vogt, S. S., Allen, S. L., Bigelow, B. C., et al. 1994, *Proc. SPIE*, **2198**, 362
- Vogt, S. S., Radovan, M., Kibrick, R., et al. 2014, *PASP*, **126**, 359
- Wahl, S. M., Hubbard, W. B., Militzer, B., et al. 2017, *GeoRL*, **44**, 4649
- Wang, J., Fischer, D. A., Barclay, T., et al. 2015, *ApJ*, **815**, 127
- Weiss, L. M., Dai, F., Huber, D., et al. 2021, *AJ*, **161**, 56
- Winn, J. N. 2010, in *Exoplanets*, ed. S. Seager (Tucson: Univ. of Arizona Press), 55
- Winn, J. N., Howard, A. W., Johnson, J. A., et al. 2009, *ApJ*, **703**, 2091
- Wittenmyer, R. A., Wang, S., Horner, J., et al. 2020, *MNRAS*, **492**, 377
- Wittrock, J. M., Kane, S. R., Horch, E. P., et al. 2016, *AJ*, **152**, 149
- Wong, M. H., Mahaffy, P. R., Atreya, S. K., Niemann, H. B., & Owen, T. C. 2004, *Icar*, **171**, 153
- Wu, Y., & Lithwick, Y. 2011, *ApJ*, **735**, 109
- Wu, Y., & Murray, N. 2003, *ApJ*, **589**, 605
- Yao, X., Pepper, J., Gaudi, B. S., et al. 2021, *AJ*, **161**, 124
- Yee, J. C., & Gaudi, B. S. 2008, *ApJ*, **688**, 616